

Stellar Chromospheric Activity Database of Solar-like Stars Based on the LAMOST Low-Resolution Spectroscopic Survey

WEITAO ZHANG,¹ JUN ZHANG,¹ HAN HE,^{2,3} ZHIPING SONG,¹ ALI LUO,^{4,3} AND HAOTONG ZHANG^{4,3}

¹*School of Physics and optoelectronics engineering, Anhui University, Hefei 230601, China*

²*CAS Key Laboratory of Solar Activity, National Astronomical Observatories, Chinese Academy of Sciences, Beijing 100101, China*

³*University of Chinese Academy of Sciences, Beijing 100049, China*

⁴*CAS Key Laboratory of Optical Astronomy, National Astronomical Observatories, Chinese Academy of Sciences, Beijing 100101, China*

ABSTRACT

A stellar chromospheric activity database of solar-like stars is constructed based on the Large Sky Area Multi-Object Fiber Spectroscopic Telescope (LAMOST) Low-Resolution Spectroscopic Survey (LRS). The database contains spectral bandpass fluxes and indexes of Ca II H&K lines derived from 1,330,654 high-quality LRS spectra of solar-like stars. We measure the mean fluxes at line cores of the Ca II H&K lines using a 1 Å rectangular bandpass as well as a 1.09 Å full width at half maximum (FWHM) triangular bandpass, and the mean fluxes of two 20 Å pseudo-continuum bands on the two sides of the lines. Three activity indexes, S_{rec} based on the 1 Å rectangular bandpass, and S_{tri} and S_L based on the 1.09 Å FWHM triangular bandpass, are evaluated from the measured fluxes to quantitatively indicate the chromospheric activity level. The uncertainties of all the obtained parameters are estimated. We also produce spectrum diagrams of Ca II H&K lines for all the spectra in the database. The entity of the database is composed of a catalog of spectral sample and activity parameters, and a library of spectrum diagrams. Statistics reveal that the solar-like stars with high level of chromospheric activity ($S_{\text{rec}} > 0.6$) tend to appear in the parameter range of T_{eff} (effective temperature) < 5500 K, $4.3 < \log g$ (surface gravity) < 4.6 , and $-0.2 < [\text{Fe}/\text{H}]$ (metallicity) < 0.3 . This database with more than one million high-quality LAMOST LRS spectra of Ca II H&K lines and basal chromospheric activity parameters can be further used for investigating activity characteristics of solar-like stars and solar-stellar connection.

Keywords: Astronomy databases (83); Sky surveys (1464); Solar-like stars (1941); Spectroscopy (1558); Stellar activity (1580); Stellar chromospheres (230)

1. INTRODUCTION

With detailed observations of solar activity for several centuries, many features and phenomena of the Sun, such as sunspots, plagues, flares, etc., have been discovered and thoroughly studied. These features and phenomena are the manifestations of magnetic field activity on the Sun (Hale 1908). Observations for solar-like stars (Cayrel de Strobel 1996) revealed that magnetic activity is also common on other stars, and the connection between stellar activity and solar activity (i.e., solar-stellar connection) has become a topic of wide interest (Noyes 1996). Choudhuri (2017) collected various stellar activity data and explored the extrapolation of solar dynamo models for explaining magnetic activity of solar-like stars. The knowledge of activity of solar-like stars in turn is very helpful for understanding the activity status of the Sun (Güdel 2007). According to the classification by Gomes da Silva et al. (2021), the Sun is located in the high-variability region of the inactive main sequence star zone. Reinhold et al. (2020) illustrated that the Sun is less active compared with other solar-like stars.

Stellar activity is closely related with the rotation period (e.g., Noyes et al. 1984b; Wright & Drake 2016; Zhang et al. 2020a) and age (e.g., Mamajek & Hillenbrand 2008; Lorenzo-Oliveira et al. 2018; Zhang et al. 2019) of stars. In general,

stellar activity level will decrease with increase in stellar rotation period or age. On the other hand, Maehara et al. (2012) found that the maximum energy of stellar flares is not correlated with stellar rotation period. Investigation on the relation between stellar activity cycle and rotation by Reinhold et al. (2017) reveals that the activity cycle period slightly increases for longer rotation period.

As an important aspect of stellar activity, the chromospheric activity of solar-like stars has always been a popular research subject (Hall 2008). A detailed review of stellar chromosphere modelling and spectroscopic diagnostics has been given by Linsky (2017). Stellar chromospheric activity of solar-like stars can be indicated by line core emissions of the Ca II H&K lines in violet band of the visible spectrum (e.g., Baliunas et al. 1995; Hall et al. 2007), the H α line in red band (e.g., Delfosse et al. 1998; Newton et al. 2017), and the Ca II infrared triplet (Ca II IRT) lines (e.g., Soderblom et al. 1993; Notsu et al. 2015), etc. The emission of Ca II H&K lines of the Sun has long been known to have a strong correlation with the solar chromospheric activity (see a comprehensive review by Linsky & Avrett 1970). With the discovery of the emissions of Ca II H&K lines from other stars (e.g., Eberhard & Schwarzschild 1913), people began to explore whether it comes from the same mechanism as the solar activity and whether it has a long-term cyclic variation as the solar cycle. Wilson (1963) at the Mount Wilson Observatory (MWO) investigated the relationship between intensity of stellar Ca II H&K emission and stellar physical nature, and concluded that the chromospheric activity of main sequence stars decreases with age. Wilson (1978) found the long-term cyclic variations of stellar Ca II H&K fluxes similar to the solar cycle. Baliunas et al. (1995) presented continuous Ca II H&K emission records of stellar chromospheric activity for 111 stars, which came from a long-term observing program at MWO. At that time, the MWO S index was first introduced as a quantitative chromospheric activity indicator based on the Ca II H&K lines (Wilson 1968; Vaughan et al. 1978; Duncan et al. 1991; Baliunas et al. 1995), defined as the ratio between the flux of Ca II H&K line cores and the flux of the reference bands on the violet and red sides of the lines multiplied by a scaling factor for calibration between different instruments. Because of the high correlation between Ca II H&K emission and stellar magnetic activity (e.g., Saar & Schrijver 1987), researchers prefer to characterize stellar magnetic activity through the indicators derived from Ca II H&K lines which often involve S index.

The S index has been established as a fundamental parameter of stellar chromosphere activity. Based on S index, by subtracting the photospheric contribution to Ca II H&K flux, the true chromospheric emission of Ca II H&K lines can be extracted as an index R'_{HK} (Linsky et al. 1979; Noyes et al. 1984a). Considering the existence of the basal (lower-limit) flux of chromosphere (Schrijver 1987) which is thought to be unrelated with magnetic activity, Mittag et al. (2013) proposed a new index R_{HK}^+ to reflect pure stellar chromospheric activity.

The Large Sky Area Multi-Object Fiber Spectroscopic Telescope (LAMOST, also named Guoshoujing Telescope) is a telescope dedicated for spectroscopic sky survey. There are 4000 fibers within a diameter of 1.75 meters (corresponding to 5° in the sky) at the focal surface (Cui et al. 2012). The Low-Resolution Spectroscopic Survey (LRS) of LAMOST began in October 2011, with a spectral resolving power ($R = \lambda/\Delta\lambda$) of about 1800 and a wavelength coverage of 3700–9100 Å (Zhao et al. 2012). The first year observation was for the pilot survey (Luo et al. 2012; Zhao et al. 2012), and the regular survey began in September 2012. LAMOST also conduct regular Medium-Resolution Spectroscopic Survey (MRS; $R \sim 7500$) since 2018 for wavelength bands of 4950–5350 Å and 6300–6800 Å (Liu et al. 2020). When completing seven years of sky survey (one year pilot survey and six years regular survey) in June 2018, LAMOST became the first spectral sky survey project in the world to accumulate more than 10 million spectra.

The majority of the released data by LAMOST is LRS spectra. The huge data set is very beneficial for big-data analyses of stellar properties. There are millions of LRS spectra of solar-like stars that can be used for studying stellar chromospheric activity and solar-stellar connection. Figure 1 gives an example of LRS spectra of solar-like stars observed by LAMOST. As illustrated in Figure 1, the LRS spectrum contains several optical spectroscopic features that can indicate stellar chromospheric activity, in which the Ca II H&K lines (highlighted in red) are the most commonly employed spectral lines. The other lines (H α and Ca II IRT) can also be used (e.g., Frasca et al. 2016), but those lines are relatively narrow and hence are not well-resolved in LRS spectra compared with Ca II H&K lines.

The massive amount of LAMOST LRS spectral data provides a great opportunity for investigating overall chromospheric activity properties of solar-like stars based on the Ca II H&K lines. Karoff et al. (2016) selected 5,648 solar-like stars (including 48 superflare stars) from LAMOST LRS catalog and studied the relation between stellar chromospheric activity level (indicated by the Ca II H&K S index) and occurrence of superflares. Zhang et al. (2020a) calculated chromospheric S index and R_{HK}^+ index of 59,816 stars from the LRS spectra of the LAMOST-*Kepler* observation project (De Cat et al. 2015; Zong et al. 2018; Fu et al. 2020) and investigated the relationship between stellar chromospheric activity and photospheric activity (indicated by the stellar light curves observed by *Kepler* space tele-

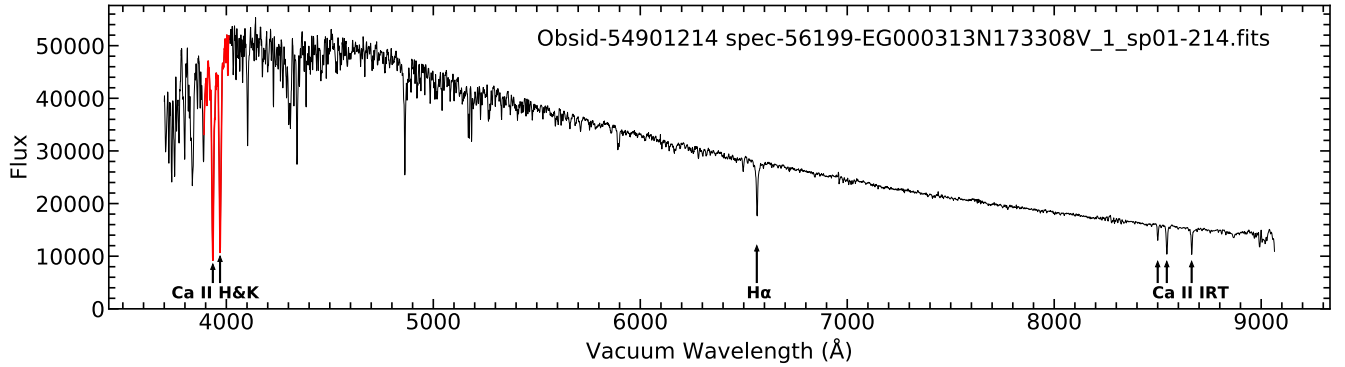


Figure 1. An example of LAMOST LRS spectrum of solar-like stars. The spectral lines commonly used for analyzing stellar chromospheric activity (Ca II H&K, H α , and Ca II IRT) are labeled. The Ca II H&K lines employed in this work are highlighted in red. The obsid (observation identifier) and FITS file name of the spectrum are shown in the plot for reference.

scope) of F-, G-, and K-type stars and the dependence of the activities on stellar rotation. Zhao et al. (2015) presented measurements of chromospheric S index for 119,995 F, G and K stars by using the LRS spectra from the first data release of LAMOST. Tu et al. (2021) found 7,454 solar-like stars with both light-curve observation by the Transiting Exoplanet Survey Satellite (TESS; Ricker et al. 2015) and LRS spectral observation by LAMOST and investigated the relations between the stellar chromospheric activity (measured by S index), photometric variability, and flare activity of the stellar objects.

The previous works discussed above used a subset of the released LAMOST spectra. We believe that exploiting the full data set of LAMOST will further facilitate the relevant research (He et al. 2021). By utilizing the large volume of LRS spectra in LAMOST Data Release 7, we constructed a stellar chromospheric activity database of solar-like stars based on the Ca II H&K lines, which is elaborated in this paper. We introduce the LAMOST Data Release 7 in Section 2 and explain the criteria for selecting high-quality LRS spectra of solar-like stars in Section 3. The data processing workflow for the selected LRS spectra and the derivation of stellar chromospheric activity measures and indexes are described in detail in Section 4. The components of the stellar chromospheric activity database of solar-like stars are elucidated in Section 5. We discuss the results obtained from the database and perform a statistical analysis of the stellar chromospheric activity indexes in Section 6. In Section 7, we summarize this work and prospect the further researches based on the database.

2. DATA RELEASE OF LAMOST

The annual observation of the LAMOST sky survey begins in September of each year and ends in June of the next year. The summer season (from July to August) is for instrument maintenance. The acquired data by LAMOST are also released in yearly increments. Each data release (DR) consists of the data files of one-dimensional spectra (in FITS format) and the catalog files (in both FITS and CSV formats) of spectroscopic parameters (Luo et al. 2015). A new DR contains all the data collected in the corresponding observing year as well as in the previous years.

The LAMOST Data Release 7 (DR7) is opened to the public in September 2021, which contains the spectral data observed from October 2011 to June 2019. In this work, we utilize the LRS spectra in LAMOST DR7 v2.0¹ to construct the stellar chromospheric activity database of solar-like stars. As demonstrated in Figure 1, the flux of LRS spectra is calibrated, and the vacuum wavelength is adopted in LAMOST data. Most telluric lines in red band of LRS spectra have been removed (Luo et al. 2015).

Basic information of the LRS spectra in LAMOST DR7 v2.0 is shown in Table 1. The spectra of solar-like stars investigated in this work are taken from the LAMOST LRS Stellar Parameter Catalog of A, F, G and K Stars (hereafter referred to as LAMOST LRS AFGK Catalog, for short), which consists of 48 spectroscopic parameters, such as observation identifier (obsid), sky coordinates, signal-to-noise ratio (SNR), magnitude, and so on. Several important stellar parameters, including effective temperature (T_{eff}), surface gravity ($\log g$), metallicity ($[\text{Fe}/\text{H}]$), and radial velocity (V_r), are also provided by the catalog. The four stellar parameters are obtained by the LAMOST Stellar Parameter

¹ <http://www.lamost.org/dr7/v2.0/>

Table 1. Basic information of the LRS spectra in LAMOST DR7 v2.0.

Classification of LRS spectra	Number of LRS Spectra
Total Released Spectra	10,431,197
Stellar Spectra	9,846,793
Stellar Spectra with SNR_g or $\text{SNR}_i > 10$	8,912,384
Stellar Spectra with AFGK Stellar Parameters	6,179,327
High-Quality Spectra of Solar-like Stars*	1,330,654

NOTE—The first four rows are taken from LAMOST DR7 v2.0. SNR_g and SNR_i mean signal-to-noise ratio in g band and i band (see Section 3 for an explanation), respectively. The number of high-quality LRS spectra of solar-like stars (labeled with a ‘*’ symbol) is obtained in this work (see Section 3 for details).

Pipeline (LASP), in which all the parameters are determined simultaneously by minimizing the squared difference between the observed spectra and the model spectra (Wu et al. 2011; Luo et al. 2015). The targets in LAMOST DR7 have been cross-matched with the Gaia DR2 catalog (Gaia Collaboration et al. 2018), and their Gaia source identifiers and G magnitudes are included in the LAMOST DR7 catalogs.

3. SELECTION OF HIGH-QUALITY LRS SPECTRA OF SOLAR-LIKE STARS

High-quality LAMOST LRS spectra of solar-like stars (Cayrel de Strobel 1996) are expected in this work. The Sun is a main-sequence star with spectral class of G2, T_{eff} of about 5800 K, and $\log g$ of about 4.4 (g in unit of $\text{cm} \cdot \text{s}^{-2}$). There are various definitions for solar-like stars in the literature with different ranges of stellar parameters around the values of the Sun (e.g., Schaefer et al. 2000; Maehara et al. 2012; Shibayama et al. 2013; Zhao et al. 2015; Reinhold et al. 2020; Zhang et al. 2020a,b). In this work, we consider the concept of solar-like stars from the viewpoint of stellar chromospheric activity and adopt a broader range of spectral class than G-type, since Ca II H&K lines are also prominent in spectra of late F- and early K-type stars (e.g., Kesseli et al. 2017).

We select high-quality LRS spectra of solar-like stars from the LAMOST LRS AFGK Catalog of LAMOST DR7 v2.0, which contains 6,179,327 LRS spectra (see Table 1) with determined stellar parameters (T_{eff} , $\log g$, $[\text{Fe}/\text{H}]$, and V_r) by the LASP. The criteria for the spectral data selection involve five aspects: SNR condition, T_{eff} range, $[\text{Fe}/\text{H}]$ range, main-sequence star condition, and data completeness in Ca II H&K band. The SNR and data completeness criteria are for the high-quality data, and the T_{eff} , $[\text{Fe}/\text{H}]$, and main-sequence star criteria are for the sample of solar-like stars. These criteria are described as follows.

1. One major indicator of the quality of a spectrum is the SNR. LAMOST catalogs provide SNR parameters for LRS spectra in five color bands, that is, ultraviolet, green, red, near infrared, and infrared bands, which are abbreviated as u , g , r , i , and z , respectively.² In LAMOST catalogs, the value of SNR is in the range from 0 to 1000. Higher SNR generally means higher quality of the spectral data, and hence smaller uncertainties of the spectral fluxes, determined stellar parameters, and derived stellar chromospheric activity parameters. In this work, we utilize the SNR parameters of LRS spectra in the g band and r band³ (denoted by SNR_g and SNR_r , respectively), and adopt the SNR condition for high-quality LRS spectra as $\text{SNR}_g \geq 50.00$ and $\text{SNR}_r \geq 71.43$. This criterion is a compromise between a smaller uncertainty of spectral fluxes/stellar parameters/activity parameters and a larger volume of spectral sample. The g -band threshold ($\text{SNR}_g \geq 50.00$) is the primary condition; the r -band threshold ($\text{SNR}_r \geq 71.43$) is determined from the g -band condition in consideration that $\text{SNR}_r/\text{SNR}_g \sim 10/7$ for the spectra with T_{eff} in the range of solar-like stars (see criterion 2). Figure 2 shows the scatter plot of SNR_g vs. SNR_r , in which the ratio of $\text{SNR}_r/\text{SNR}_g = 10/7$ and the SNR thresholds for high-quality spectra are illustrated.

² The $ugriz$ color bands have been adopted by the Sloan Digital Sky Survey (SDSS) (Stoughton et al. 2002).

³ The wavelength ranges of the g band and r band are 3620–5620 Å and 5380–7040 Å, respectively (Doi et al. 2010).

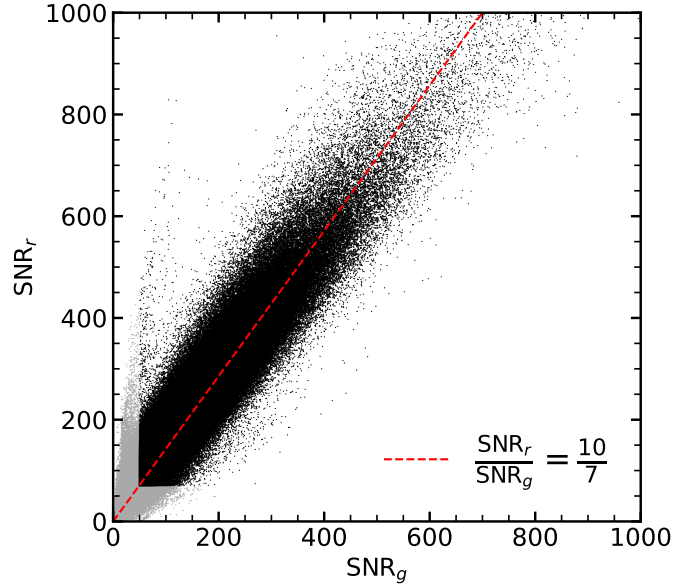


Figure 2. Scatter plot of SNR_g vs. SNR_r for the spectra in the LAMOST LRS AFGK Catalog with T_{eff} in the range of 4800–6800 K. The black dots represent the high-quality spectra with $\text{SNR}_g \geq 50.00$ and $\text{SNR}_r \geq 71.43$. The gray dots represent the spectra with SNR_g or SNR_r below the thresholds. The dashed line indicates the ratio of $\text{SNR}_r/\text{SNR}_g = 10/7$.

It should be noted that although the Ca II H&K lines employed in this work are in the g band, the whole LRS spectrum is used by the LASP to determine the stellar parameters (Luo et al. 2015). In addition to the g -band SNR condition, the r -band SNR condition is included to ensure a smaller uncertainty of stellar parameters.

2. The range of T_{eff} for solar-like stars is adopted as $4800 \text{ K} \leq T_{\text{eff}} \leq 6800 \text{ K}$, which is around the effective temperature of the Sun ($\sim 5800 \text{ K}$) with fluctuation of $\pm 1000 \text{ K}$. The main-sequence stars with T_{eff} in this range presents prominent Ca II H&K lines in their spectra (e.g., Kesseli et al. 2017) and hence are considered as candidates of solar-like stars; they belong to late F-type, G-type, and early K-type stars.
3. The range of $[\text{Fe}/\text{H}]$ for solar-like stars is adopted as $-1.0 < [\text{Fe}/\text{H}] < 1.0$, which is around the metallicity of the Sun ($[\text{Fe}/\text{H}] = 0.0$). The stars with $[\text{Fe}/\text{H}]$ less than -1.0 (metal-poor stars) might have a different origin from the Sun (e.g., Frebel & Norris 2015) and hence are not considered to be solar-like.
4. In the $T_{\text{eff}} - \log g$ diagram of stellar objects, main-sequence stars distribute in the horizontal branch and giant stars are in the erect branch. Base on the $T_{\text{eff}} - \log g$ diagram of the spectra in the LAMOST LRS AFGK Catalog, as shown in Figure 3, we adopt the following empirical formula to distinguish the spectra of main-sequence stars in the T_{eff} range of 4800–6800 K:

$$\log g \geq 5.98 - 0.00035 \times T_{\text{eff}} \quad \text{for } 4800 \text{ K} \leq T_{\text{eff}} \leq 6800 \text{ K}. \quad (1)$$

The separation line between the giant and main-sequence samples defined by Equation (1) is shown as a black solid line ($\log g = 5.98 - 0.00035 \times T_{\text{eff}}$) in Figure 3. The two endpoints of the line, ($T_{\text{eff}} = 6800 \text{ K}$, $\log g = 3.6$) and ($T_{\text{eff}} = 4800 \text{ K}$, $\log g = 4.3$), are determined empirically by visual inspecting the distribution of the LRS samples in the $T_{\text{eff}} - \log g$ diagram. In Figure 3, the sample of main-sequence stars (beneath the black solid line, as according to Equation (1)) with T_{eff} in the range of 4800–6800 K (criterion 2) and SNR above the thresholds (criterion 1) is shown in green; the sample of giant stars (above the black solid line) with SNR above the thresholds is shown in orange; the sample of other main-sequence stars ($T_{\text{eff}} < 4800 \text{ K}$ or $T_{\text{eff}} > 6800 \text{ K}$) with SNR above the thresholds is shown in blue; and the sample below the SNR thresholds is shown in gray.

5. In this work, we utilize the Ca II H&K band to analyze stellar chromospheric activity. Some LRS spectral data in this band contain data points with zero or negative fluxes, which are not reliable according to the caveat of

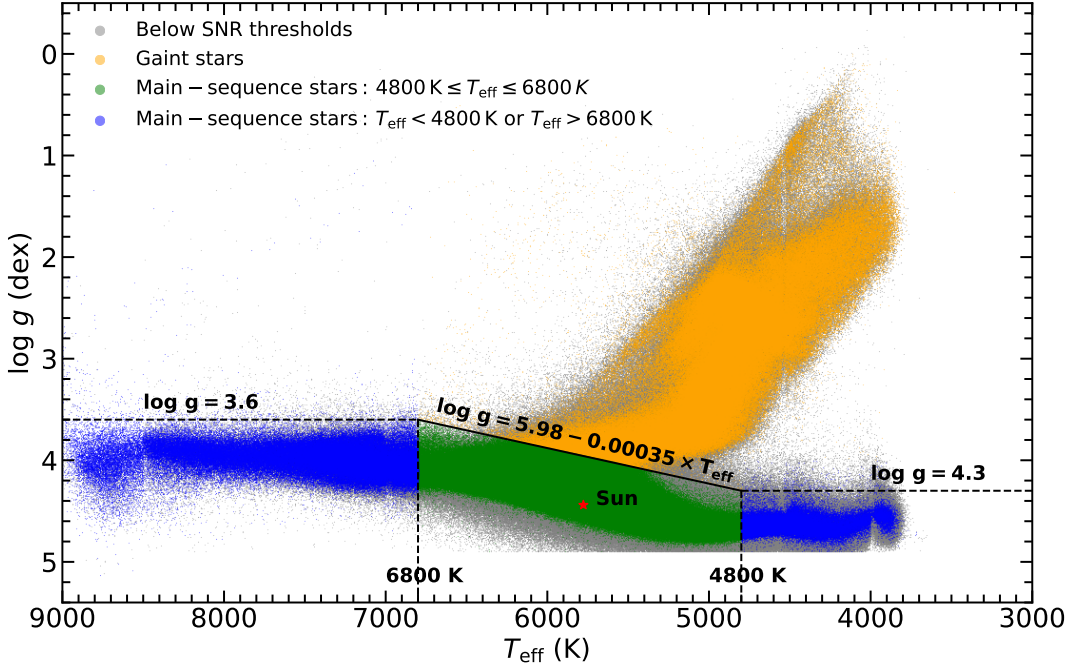


Figure 3. T_{eff} - $\log g$ diagram of the spectra contained in the LAMOST LRS AFGK Catalog. The black solid line is defined by Equation (1) and divides the samples of main-sequence stars (beneath the line) and giant stars (above the line). The sample with SNR below the thresholds (see criterion 1 in Section 3) is shown in gray. The sample with SNR above the thresholds is shown in color, in which the sample of main-sequence stars with $4800 \text{ K} \leq T_{\text{eff}} \leq 6800 \text{ K}$ (solar-like candidates) is shown in green, the sample of other main-sequence stars ($T_{\text{eff}} < 4800 \text{ K}$ or $T_{\text{eff}} > 6800 \text{ K}$) is in blue, and the sample of giant stars is in orange. The position of solar T_{eff} and $\log g$ is indicated with a ‘ \star ’ symbol.

LAMOST and should be removed from the spectral data. Those LRS spectra with incomplete data points in Ca II H&K band are not used in the analysis.

By applying the first four criteria (SNR condition, T_{eff} range, $[\text{Fe}/\text{H}]$ range, and main-sequence star condition) for the spectra in the LAMOST LRS AFGK Catalog, we get a sample of 1,352,910 LRS spectra. By applying the fifth criterion (data completeness in Ca II H&K band), 22,256 spectra in the sample are discarded. We ultimately obtain 1,330,654 high-quality LAMOST LRS spectra of solar-like stars that are suitable for studying stellar chromospheric activity through the Ca II H&K lines. The number density distribution of these selected LRS spectra in the T_{eff} - $\log g$ parameter space is shown in Figure 4. The sky coordinates of these selected spectra are illustrated in Figure 5.

In Figure 6, we show the distributions of the uncertainty values of the four stellar parameters determined by the LASP (denoted by δT_{eff} , $\delta \log g$, $\delta[\text{Fe}/\text{H}]$, and δV_r , respectively) for all the selected high-quality LRS spectra of solar-like stars. It can be seen from Figure 6 that the peak positions of the uncertainty distributions of the four stellar parameters are $\delta T_{\text{eff}} \sim 25 \text{ K}$, $\delta \log g \sim 0.035 \text{ dex}$, $\delta[\text{Fe}/\text{H}] \sim 0.025 \text{ dex}$, and $\delta V_r \sim 3.5 \text{ km/s}$, respectively. The high-accurate stellar parameters of the selected LRS spectra of solar-like stars lay a good foundation for the subsequent data processing and analysis.

4. DATA PROCESSING WORKFLOW FOR THE SELECTED LRS SPECTRA OF SOLAR-LIKE STARS

The purpose of data processing is to obtain emission fluxes of Ca II H&K lines and chromospheric activity indexes for each of the selected LRS spectra of solar-like stars. The workflow for data processing has four steps (He et al. 2021): (1) correction for wavelength shift introduced by radial velocity; (2) measurement of emission fluxes of Ca II H&K lines; (3) evaluation of chromospheric activity indexes; and (4) estimation of uncertainties of emission flux measures and activity indexes. These steps are described in detail in the following subsections.

4.1. Correction for Wavelength Shift Introduced by Radial Velocity

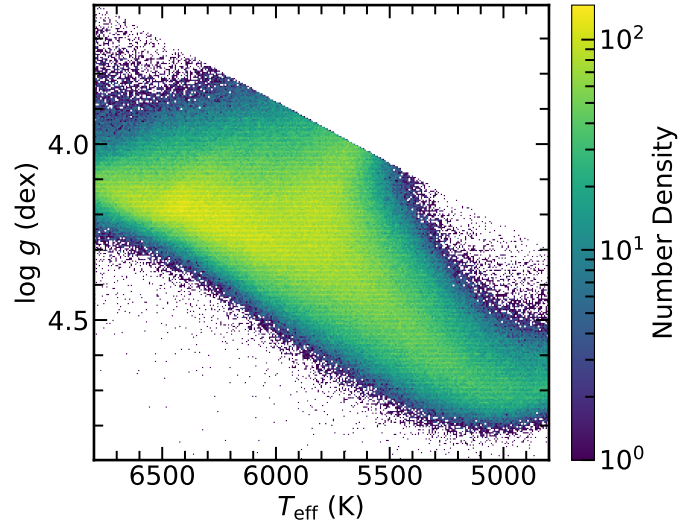


Figure 4. Number density distribution of all the selected high-quality LAMOST LRS spectra of solar-like stars in the T_{eff} - $\log g$ parameter space.

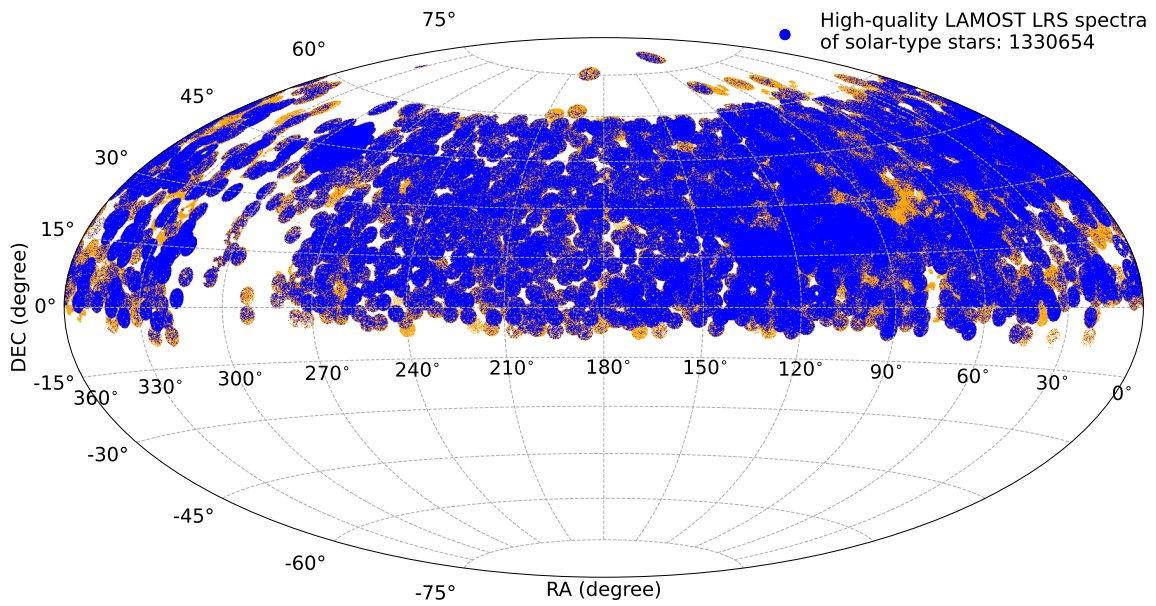


Figure 5. Diagram illustrating sky coordinates of all the selected high-quality LAMOST LRS spectra of solar-like stars (blue dots). The original sample in the LAMOST LRS AFGK Catalog is also depicted for reference (in orange and beneath the blue dots).

The radial velocity of a stellar object causes wavelength shift in the observed spectrum. This wavelength shift should be corrected to obtain the spectrum in rest frame before measuring the emission fluxes of Ca II H&K lines. The radial velocity values of the selected LRS spectra of solar-like stars have been determined by the LASP and are provided by the LAMOST LRS AFGK Catalog.

The relation between the radial velocity V_r and the wavelength shift of a spectrum can be expressed as

$$\frac{\lambda - \lambda_0}{\lambda_0} = \frac{V_r}{c}, \quad (2)$$

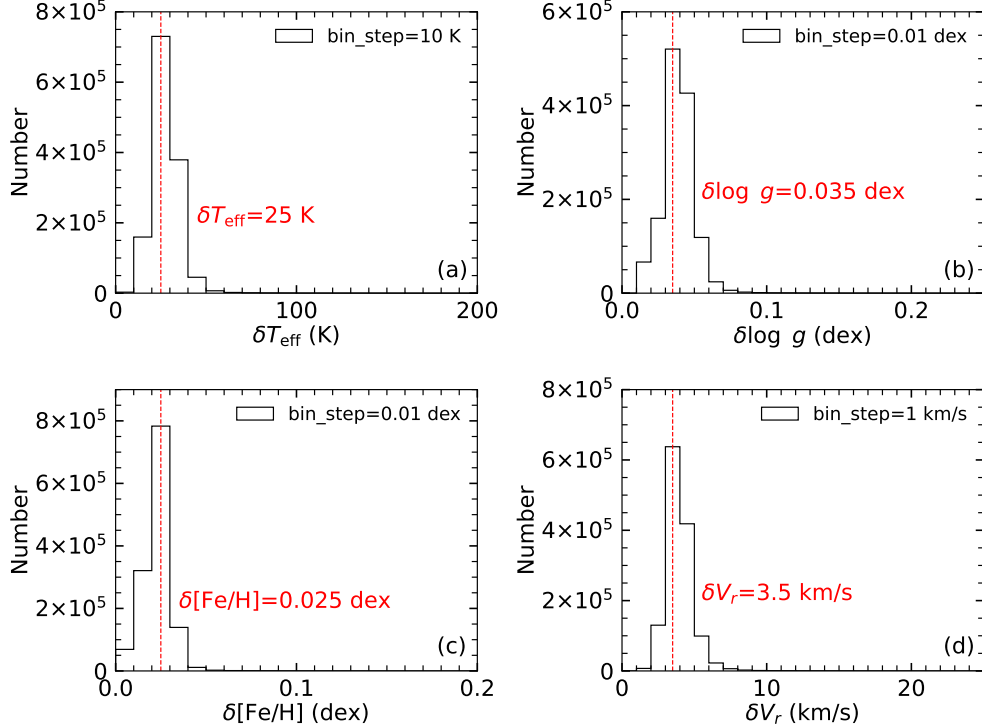


Figure 6. Histograms of the uncertainty values of (a) T_{eff} , (b) $\log g$, (c) $[\text{Fe}/\text{H}]$, and (d) V_r for all the selected high-quality LAMOST LRS spectra of solar-like stars. The vertical dashed line in each plot indicates the peak position of the uncertainty distribution, and the value of the peak position is labeled.

where c is the speed of light, λ is the wavelength value of the observed spectrum, λ_0 is the wavelength value in rest frame, and $\lambda - \lambda_0$ is the wavelength shift introduced by radial velocity. Then, the desired wavelength value in rest frame, λ_0 , can be calculated from the observed wavelength value λ and radial velocity V_r by the following equation:

$$\lambda_0 = \frac{\lambda}{1 + \frac{V_r}{c}}. \quad (3)$$

An example of wavelength shift correction for Ca II H&K lines in LAMOST LRS spectra can be seen in Figure 9.

4.2. Measurement of Emission Fluxes of Ca II H&K lines

The first long-term program of measuring emission fluxes of stellar Ca II H&K lines for a bulk of stars started in 1966 at MWO (Wilson 1968) using a photoelectric scanner called HKP-1. When a new photoelectric spectrometer referred to as HKP-2 was constructed at MWO, Vaughan et al. (1978) formally defined the H , K , R and V channels of Ca II H&K lines and began to routinely measure stellar emission fluxes in the four bands. The H and K bands are two 1.09 \AA full width at half maximum (FWHM) triangular bandpasses at line cores of Ca II H and K lines (center wavelengths in air being 3968.47 \AA and 3933.66 \AA , respectively), and the R and V bands are two 20 \AA rectangular bandpasses on the red and violet sides of the Ca II H&K lines (wavelength ranges in air being $3991.07\text{--}4011.07 \text{ \AA}$ and $3891.07\text{--}3911.07 \text{ \AA}$, respectively). The R and V bands provide reference fluxes of pseudo-continuum for evaluation of S index (Vaughan et al. 1978; Duncan et al. 1991).

The aforementioned H , K , R , and V bands have become the standard for characterizing emissions of Ca II H&K lines and been widely used for assessing stellar chromospheric activity in the literature (e.g., Hall et al. 2009; Isaacson & Fischer 2010; Mittag et al. 2013; Beck et al. 2016; Salabert et al. 2016; Boro Saikia et al. 2018; Karoff et al. 2019; Melbourne et al. 2020; Zhang et al. 2020a; Gomes da Silva et al. 2021; Sowmya et al. 2021). Meanwhile, researchers also look for alternative definitions of the bands to quantify the emissions of Ca II H&K lines for specific facilities and data sets. For example, Zhao et al. (2013) defined their H and K bands as 2 \AA rectangular bandpasses for the spectral data of SDSS; Mittag et al. (2016) adopted 1 \AA rectangular H and K bands for the spectral data of the TIGRE telescope. Both Zhao et al. (2013) and Mittag et al. (2016) kept the definitions of R and V bands by MWO.

Table 2. Emission flux measures of Ca II H&K lines.

Measure	Column in Database		Description	Center Wavelength	
				(in Air)	(in Vacuum)
\tilde{R}	R_mean		Mean flux in R band (20 Å rectangular bandpass)	4001.07 Å	4002.20 Å
\tilde{V}	V_mean		Mean flux in V band (20 Å rectangular bandpass)	3901.07 Å	3902.17 Å
\tilde{H}_{tri}	H_mean_tri		Mean flux in H band with 1.09 Å FWHM triangular bandpass	3968.47 Å	3969.59 Å
\tilde{K}_{tri}	K_mean_tri		Mean flux in K band with 1.09 Å FWHM triangular bandpass	3933.66 Å	3934.78 Å
\tilde{H}_{rec}	H_mean_rec		Mean flux in H band with 1 Å rectangular bandpass	3968.47 Å	3969.59 Å
\tilde{K}_{rec}	K_mean_rec		Mean flux in K band with 1 Å rectangular bandpass	3933.66 Å	3934.78 Å

NOTE— ‘Column in Database’ is used in Section 5.1. The wavelengths in air are taken from Vaughan et al. (1978). The wavelengths in vacuum are calculated from air wavelengths using the formula given by Ciddor (1996).

In this work, we adopt the classical definitions of R and V bands with 20 Å rectangular bandpasses, the classical definitions of H and K bands with 1.09 Å FWHM triangular bandpasses, and the alternative definitions of H and K bands with 1 Å rectangular bandpasses for the LAMOST LRS spectra. Six emission flux measures are introduced to evaluate the mean fluxes in the six bandpasses, which are tabulated in Table 2. These measures are \tilde{R} and \tilde{V} for the mean fluxes in the 20 Å wide R and V reference bands, \tilde{H}_{tri} and \tilde{K}_{tri} for the mean fluxes in the H and K bands with 1.09 Å FWHM triangular bandpasses, and \tilde{H}_{rec} and \tilde{K}_{rec} for the mean fluxes in the H and K bands with 1 Å rectangular bandpasses. \tilde{H}_{rec} and \tilde{K}_{rec} are measured for Ca II H&K lines in addition to \tilde{H}_{tri} and \tilde{K}_{tri} because the physical meaning of the fluxes in rectangular bandpass are more straightforward than the fluxes in triangular bandpass (see further discussion on the two types of bandpasses in Section 6.1).

The center wavelength values of the R , V , H , and K bands are given in the rightmost two columns of Table 2. The wavelength values in air are taken from Vaughan et al. (1978), and the wavelength values in vacuum are calculated from the air wavelengths by using the conversion formula given by Ciddor (1996). In practical computation, the vacuum wavelengths are employed to derive the six emission flux measures from the LAMOST LRS spectra. A diagram illustration of the vacuum wavelength ranges of the 20 Å wide R and V bands, the 1.09 Å FWHM triangular H and K bands, and the 1 Å rectangular H and K bands can be found in Figure 9.

We derive the values of the six emission flux measures (\tilde{R} , \tilde{V} , \tilde{H}_{tri} , \tilde{K}_{tri} , \tilde{H}_{rec} , and \tilde{K}_{rec}) of Ca II H&K lines for all the selected LRS spectra of solar-like stars. To measure the mean flux in a bandpass for a LAMOST LRS spectrum, we first integrate the spectral fluxes in the bandpass, and then divide the integrated flux value by the wavelength width of the bandpass. Since the LRS spectrum consists of discrete data points which are a bit sparse for the bandpass integration, we obtain a denser distribution of data points in the bandpass via linear interpolation. The wavelength steps after interpolation are 0.01 Å for R and V bands and 0.001 Å for H and K bands. Then, the mean flux value in a bandpass is calculated based on the interpolated spectral data.

4.3. Evaluation of Chromospheric Activity Indexes

From the emission flux measures of Ca II H&K lines obtained in Section 4.2, stellar chromospheric activity indexes can be evaluated. The widely used chromospheric activity indicator, the classical MWO S index (denoted by S_{MWO}), was originally defined at MWO as (Wilson 1968; Vaughan et al. 1978; Duncan et al. 1991; Baliunas et al. 1995)

$$S_{\text{MWO}} = \alpha \cdot \frac{N_H + N_K}{N_R + N_V}, \quad (4)$$

where N_H and N_K are the number of counts in the 1.09 Å FWHM triangular bandpasses of Ca II H and K lines, N_R and N_V are the number of counts in the 20 Å R and V reference bands (Vaughan et al. 1978), and α is a scaling factor for adjusting the HKP-2 measurements to be in the similar scale as HKP-1 results (Duncan et al. 1991).

For the LAMOST LRS spectra, by referring to the definition of S_{MWO} , we can introduce the LAMOST S index (denoted by S_L) which is expressed as (Lovis et al. 2011; Karoff et al. 2016)

$$S_L = \alpha_L \cdot \frac{8 \times 1.09 \text{ \AA}}{20 \text{ \AA}} \cdot \frac{\tilde{H}_{\text{tri}} + \tilde{K}_{\text{tri}}}{\tilde{R} + \tilde{V}}, \quad (5)$$

where α_L is the scaling factor for LAMOST, and \tilde{H}_{tri} , \tilde{K}_{tri} , \tilde{R} , and \tilde{V} are the emission flux measures of Ca II H&K lines defined in Section 4.2 (see Table 2). The reason for multiplying 8 to the 1.09 Å FWHM is that the integration time spent on the H and K bands by the spectrometer used in MWO is eight times longer than that on the 20 Å wide R and V bands (Duncan et al. 1991; Lovis et al. 2011). The value of α_L is adopted as 1.8 for LAMOST LRS data as suggested by Karoff et al. (2016), which is determined based on the S -index distributions of solar-like stars.

The relationship between the values of S_L derived from LAMOST LRS spectra and the values of S_{MWO} measured by MWO can be calibrated based on the common stars of the two data sets. In Figure 7, we show the scatter plot of S_L vs. S_{MWO} for 65 common stars between the selected LRS spectra of solar-like stars in this work and the S_{MWO} catalog given by Duncan et al. (1991). As exhibited in Figure 7, the relationship between S_L and S_{MWO} can be fitted with an exponential function

$$S_{\text{MWO}} = e^{8.806 S_L - 3.348}, \quad (6)$$

which is displayed as a black line in Figure 7 (see Appendix A for details of the common stars and fitting procedure). The nonlinear relation is expected for larger S -index values since they are obtained by instruments with distinct spectral resolutions (see, e.g., Vaughan et al. 1978; Henry et al. 1996, for more examples). For smaller S_{MWO} values (less than 0.3), the fitted line approaches $S_{\text{MWO}}/S_L = 1$ as exhibited in Figure 7, illustrating the suitability of the scaling factor value of $\alpha_L = 1.8$ adopted for LAMOST LRS data.

The median of the relative deviations between the S_L values of the common stars and the fitted line in Figure 7 is about 8.8%. The large residuals could be due to the long-term activity variation in these stars (e.g., Wilson 1978; Baliunas & Jastrow 1990; Baliunas et al. 1995; Radick et al. 2018), and LAMOST only captures a snapshot observation of these stars' activity at all S -index values.

If the activity index values are not needed to be in the similar scale as the measurements at MWO, the factors in Equation (5) are unnecessary. Therefore, we can define the S_{tri} index

$$S_{\text{tri}} = \frac{\tilde{H}_{\text{tri}} + \tilde{K}_{\text{tri}}}{\tilde{R} + \tilde{V}} \quad (7)$$

based on the 1.09 Å FWHM triangular bandpass for Ca II H&K lines. The S_L index is connected with the S_{tri} index by equation

$$S_L = 1.8 \times \frac{8 \times 1.09 \text{ \AA}}{20 \text{ \AA}} \times S_{\text{tri}} \approx 0.785 S_{\text{tri}}. \quad (8)$$

If it is not needed to keep the bandpass shape adopted by MWO, we can also use the 1 Å rectangular bandpasses to measure the line core emissions of Ca II H&K lines (see Section 4.2) and define the S_{rec} index as

$$S_{\text{rec}} = \frac{\tilde{H}_{\text{rec}} + \tilde{K}_{\text{rec}}}{\tilde{R} + \tilde{V}}. \quad (9)$$

Jenkins et al. (2011) analyzed the influences of change in width of bandpasses at line cores of Ca II H&K lines on the result of S index. Their result showed that the correlation between the derived S -index values and the original values of MWO decreases with increasing bandpass width (such as 2 Å, 3 Å, 4 Å, etc.) even for low-resolution spectral data. Therefore, we adopt the current bandpass widths for defining the activity indexes S_{tri} , S_L , and S_{rec} to keep best compatibility with the MWO measurements.

We calculated the values of S_{tri} , S_L , and S_{rec} indexes by using Equations (7), (8), and (9) for all the selected LRS spectra of solar-like stars. The correlations between the values of the three indexes are illustrated and discussed in Section 6.1.

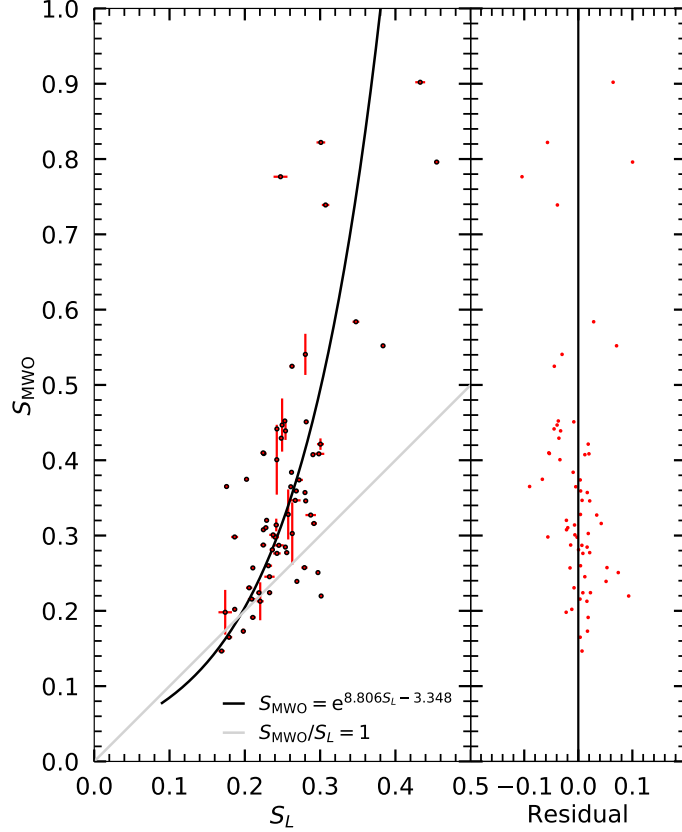


Figure 7. Scatter plot of S_L vs. S_{MWO} for 65 common stars between the selected LRS spectra of solar-like stars in this work and the S_{MWO} catalog given by Duncan et al. (1991). Error bars are displayed for the data points with known uncertainty values. The relationship between S_L and S_{MWO} is fitted with an exponential function (black line; see Appendix A for details of the common stars and fitting procedure). The gray line indicates the ratio of $S_{MWO}/S_L = 1$. Note that the fitted line approaches $S_{MWO}/S_L = 1$ for smaller S -index values.

4.4. Estimation of Uncertainties of Emission Flux Measures and Activity Indexes

In Sections 4.2 and 4.3, six emission flux measures of Ca II H&K lines and three stellar chromospheric activity indexes are derived from the LRS spectra. In this subsection, we estimate uncertainties of these activity parameters. Three sources of uncertainty are taken into account: the uncertainty of spectral flux, the discretization in spectral data, and the uncertainty of radial velocity, which can finally propagate into the composite uncertainty values of the derived activity parameters.

The FITS file of a LRS spectrum provides the value of inverse variance ($1/\delta_0^2$, where δ_0 denotes the uncertainty of flux) to indicate photon noise for each data point in the spectrum. As described in Sections 4.2 and 4.3, the emission flux measures as well as the activity indexes are calculated based on the interpolated spectral data. The flux uncertainty value of an interpolated data point (denoted by δ_i) can be derived from δ_0 by equation

$$\frac{\delta_i^2}{n_i} = \frac{\delta_0^2}{n_0}, \quad (10)$$

where n_i is number density of the spectral data after interpolation and n_0 is number density in the original LRS spectrum. Then, for a given activity parameter P (one of the six emission flux measures and three activity indexes), the uncertainty of P caused by the uncertainty of spectral flux (denoted by δP_{flux}) can be estimated from δ_i based on the definitions or formulas in Section 4.2 and 4.3 using the error propagation rules.

A spectrum is stored in discrete data points, and the flux values between data points have to be obtained via an interpolation algorithm as described in Section 4.2, which leads to uncertainties of the derived emission flux measures and activity indexes. To estimate the uncertainties of the activity parameters caused by the discretization in spectral

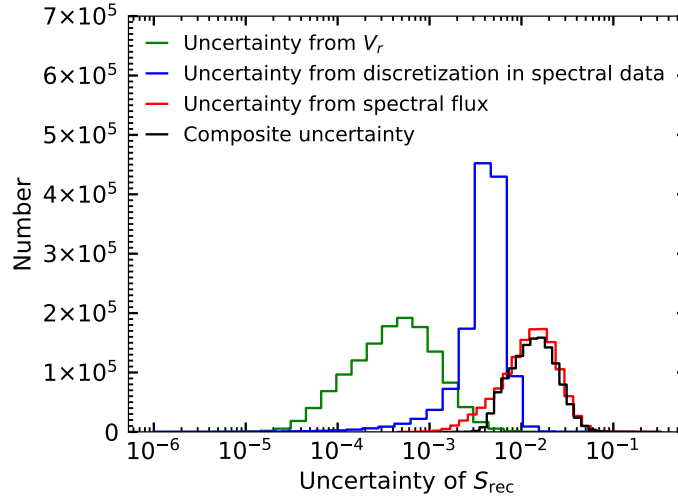


Figure 8. Distribution histograms of the uncertainties of the S_{rec} index originating from V_r uncertainty (green line), discretization in spectral data (blue line), spectral flux uncertainty (red line), and all uncertainty sources (composite uncertainty; black line).

data, we utilize two interpolation algorithm to obtain the spectral flux values between data points. One is the linear interpolation algorithm as used in Section 4.2, and another is the cubic interpolation algorithm. For a given activity parameter P , we can get two parameter values, P_{linear} and P_{cubic} , corresponding to the two interpolation algorithms, respectively. Then, the uncertainty of P caused by the discretization in spectral data (denoted by $\delta P_{\text{discrete}}$) can be estimated as the difference between P_{linear} and P_{cubic} , i.e.,

$$\delta P_{\text{discrete}} = |P_{\text{cubic}} - P_{\text{linear}}|. \quad (11)$$

To estimate the uncertainties of the emission flux measures and activity indexes caused by the uncertainty of radial velocity, we perform wavelength correction for a LRS spectrum (as described in Section 4.1) using three deliberately set radial velocity values, $V_r - \delta V_r$, V_r , and $V_r + \delta V_r$, where V_r is the formal radial velocity of the spectrum determined by LASP and δV_r is the uncertainty of the radial velocity. For a given activity parameter P , we can get three parameter values, P_- , P , and P_+ , corresponding to the three deliberately set radial velocity values, respectively. Then, the uncertainty of P caused by the uncertainty of radial velocity (denoted by δP_{V_r}) can be estimated by the following formula:

$$\delta P_{V_r} = \frac{|P_- - P| + |P_+ - P|}{2}. \quad (12)$$

The composite uncertainty of P (denoted by δP) caused by all the three uncertainty sources can be calculated by formula

$$\delta P = \sqrt{(\delta P_{\text{flux}})^2 + (\delta P_{\text{discrete}})^2 + (\delta P_{V_r})^2}. \quad (13)$$

We calculate the uncertainty values (δP_{flux} , δP_{V_r} , and δP) of the six emission flux measures and three activity indexes for all the selected LRS spectra of solar-like stars. In Figure 8, we show the relative magnitudes among the uncertainties originating from different sources, by using the uncertainty of the activity index S_{rec} as an example. As illustrated in Figure 8, the uncertainty of S_{rec} originating from the uncertainty of spectral flux (about 10^{-2}) is roughly an order of magnitude higher than that from the discretization in spectral data (about 10^{-3}), which in turn is roughly an order of magnitude higher than that from the uncertainty of radial velocity (about 10^{-4}).

All results of the obtained emission flux measures and activity indexes, and the estimated composite uncertainties of the activity parameters are integrated into the catalog of the stellar chromospheric activity database of solar-like stars (see Section 5). In a few of LRS data, the inverse variance values are not available at some data points in the H , K , R , and V bands of Ca II H&K lines. For those spectra, the uncertainty values of the emission flux measures and activity indexes are filled with ‘-9999’ in the catalog of the database.

5. STELLAR CHROMOSPHERIC ACTIVITY DATABASE OF SOLAR-LIKE STARS

In Section 3, we select 1,330,654 high-quality LRS spectra of solar-like stars from LAMOST DR7 v2.0. In Section 4, we derive six emission flux measures (\tilde{R} , \tilde{V} , \tilde{H}_{tri} , \tilde{K}_{tri} , \tilde{H}_{rec} , and \tilde{K}_{rec}) and three stellar chromospheric activity indexes (S_{tri} , S_L , and S_{rec}) of Ca II H&K lines as well as their uncertainties for the selected LAMOST LRS spectra. These emission flux measures and activity indexes can be used to investigate the overall distribution of chromospheric activity of solar-like stars as well as the activity characteristics of individual spectra. We also produce spectrum diagrams of Ca II H&K lines for all the selected LRS spectra. A stellar chromospheric activity database of solar-like stars are constructed based on the selected LAMOST LRS spectra, the derived emission flux measures and activity indexes, and the produced spectrum diagrams of Ca II H&K lines. The entity of the database is composed of a catalog of the spectral sample and activity parameters, and a library of the spectrum diagrams, which are described in detail in the following subsections. An online version of the database is available.⁴ The original FITS data files of the associated LRS spectra can be queried and downloaded from the LAMOST website (see Section 2) through the `obsid` or `fitsname` information (see Table 3) included in the catalog the database.

5.1. Catalog of Spectral Sample and Activity Parameters

The catalog of the 1,330,654 high-quality LAMOST LRS spectra of solar-like stars as well as the derived emission flux measures and activity indexes is stored in a CSV format file (filename: `CaIIHK_Sindex_LAMOST_DR7_LRS.csv`). Each row of the catalog corresponds to a LRS spectrum. All the columns in the catalog are tabulated in Table 3 with brief descriptions. As shown in Table 3, the six emission flux measures (columns: `R_mean`, `V_mean`, `H_mean_tri`, `K_mean_tri`, `H_mean_rec`, and `K_mean_rec`), the three activity indexes (columns: `S_tri`, `S_L`, and `S_rec`), and their uncertainties derived in Section 4 are included in the catalog (18 columns in total). The figure file name of Ca II H&K spectrum diagram (see Section 5.2) is also included in the catalog (column: `figname`). The aforementioned 19 columns provided by this work are labeled with a ‘*’ symbol in Table 3. Other columns in Table 3 are taken from the data release of LAMOST; those columns are used in this work and hence are kept in the catalog for reference.

Table 3. Columns in the catalog of the database.

Column	Unit	Description
<code>obsid</code>		Observation identifier of LAMOST spectrum
<code>fitsname</code>		FITS file name of LAMOST spectrum
<code>snrg</code>		SNR in g band (SNR_g)
<code>snrr</code>		SNR in r band (SNR_r)
<code>teff</code>	K	Effective temperature (T_{eff})
<code>teff_err</code>	K	Uncertainty of T_{eff}
<code>logg</code>	dex	Surface gravity ($\log g$)
<code>logg_err</code>	dex	Uncertainty of $\log g$
<code>feh</code>	dex	Metallicity ($[\text{Fe}/\text{H}]$)
<code>feh_err</code>	dex	Uncertainty of $[\text{Fe}/\text{H}]$
<code>rv</code>	km/s	Radial velocity (V_r)
<code>rv_err</code>	km/s	Uncertainty of V_r
<code>ra_obs</code>	degree	Right ascension (RA) of fiber pointing
<code>dec_obs</code>	degree	Declination (DEC) of fiber pointing
<code>gaia_source_id</code>		Source identifier in Gaia DR2 catalog
<code>gaia_g_mean_mag</code>		G magnitude in Gaia DR2 catalog
<code>figname*</code>		Figure file name of Ca II H&K spectrum diagram
<code>R_mean*</code>		Mean flux in R band (\tilde{R})

Table 3 continued on next page

⁴ <https://doi.org/10.5281/zenodo.7067044>

Table 3 (continued)

Column	Unit	Description
R_mean_err*		Uncertainty of \tilde{R}
V_mean*		Mean flux in V band (\tilde{V})
V_mean_err*		Uncertainty of \tilde{V}
H_mean_tri*		Mean flux in H band with 1.09 Å FWHM triangular bandpass (\tilde{H}_{tri})
H_mean_tri_err*		Uncertainty of \tilde{H}_{tri}
K_mean_tri*		Mean flux in K band with 1.09 Å FWHM triangular bandpass (\tilde{K}_{tri})
K_mean_tri_err*		Uncertainty of \tilde{K}_{tri}
S_tri*		S_{tri} index using 1.09 Å FWHM triangular bandpasses of H and K bands
S_tri_err*		Uncertainty of S_{tri}
S_L*		LAMOST S index (S_L)
S_L_err*		Uncertainty of S_L
H_mean_rec*		Mean flux in H band with 1 Å rectangular bandpass (\tilde{H}_{rec})
H_mean_rec_err*		Uncertainty of \tilde{H}_{rec}
K_mean_rec*		Mean flux in K band with 1 Å rectangular bandpass (\tilde{K}_{rec})
K_mean_rec_err*		Uncertainty of \tilde{K}_{rec}
S_rec*		S_{rec} index using 1 Å rectangular bandpasses of H and K bands
S_rec_err*		Uncertainty of S_{rec}

NOTE—Columns labeled with a ‘*’ symbol are provided by this work. Other columns are used in this work and are taken from the data release of LAMOST.

5.2. Library of Spectrum Diagrams

To intuitively illustrate spectral profiles, we produce spectrum diagram of Ca II H&K lines of LAMOST LRS spectra. Figure 9 shows an example of the spectrum diagrams using a LRS spectrum with obsid = 54904030. In the spectrum diagram, the original LRS spectrum is displayed with a blue dash-dot line, and the wavelength-shifted spectrum after radial velocity correction (see Section 4.1) is displayed with a red solid line. The right-hand vertical axis shows the original flux of the spectrum released by LAMOST. This original flux is normalized by its maximum value in the wavelength range of the diagram (3892.17–4012.20 Å) to yield relative flux. The relative flux after normalization is displayed in the left-hand vertical axis.

The 20 Å wide R and V pseudo-continuum bands are illustrated by two yellow rectangular regions on the right side and left side of the spectrum diagram, respectively. The 1.09 Å FWHM triangular H and K bands are indicated by two green triangular regions centered at 3969.59 Å and 3934.78 Å (wavelengths of the Ca II H and K line cores in vacuum; see Table 2), respectively. Within the triangular regions are the 1 Å rectangular H and K bands which are shown in yellow. In the title area of the spectrum diagram, the obsid, FITS file name, and data release number of the LAMOST spectrum are given in the first line, and several stellar and spectroscopic parameters used in this work (T_{eff} , $\log g$, $[\text{Fe}/\text{H}]$, SNR_g , and SNR_r) are displayed in the second line. The stellar chromospheric activity parameters derived in this work (H_mean_rec, H_mean_tri, R_mean, K_mean_rec, K_mean_tri, V_mean, S_rec, S_tri, and S_L) are shown in the area just above the spectrum plot. The radial velocity value can be seen in the upper left area of the diagram.

We produced spectrum diagrams for all the 1,330,654 LAMOST LRS spectra of solar-like stars employed by the database. These spectrum diagrams are saved as JPG format figures. All the figures constitute the library of spectrum diagrams of the database. The filenames of the figures follow the convention of ‘CaIIHK_obsid-⟨9-digit-obsid⟩_⟨primary name of FITS file⟩.jpg’ and are included in the catalog of the database (‘filename’ in Table 3). To facilitate retrieval and utilization of the spectrum diagrams, we rewrite LAMOST obsid as a 9-digit number. If the number of digits of an original obsid is less than 9, ‘0’ is padded on the left. (For example, ‘103019’ is rewritten as ‘000103019’). Diagrams with the same first three digits of the 9-digit-obsid are gathered into a folder named with the first three digits (such as



Figure 9. An example of the spectrum diagrams of Ca II H&K lines in the database using a LAMOST LRS spectrum with $\text{obsid} = 54904030$. The wavelength range of the diagram is $3892.17\text{--}4012.20 \text{ \AA}$. The original flux of the spectrum released by LAMOST is shown through the right-hand vertical axis. The left-hand vertical axis is the relative flux normalized by the maximum value of the original flux in the plot. The blue dash-dot line is the original LAMOST spectrum, and the red solid line is the wavelength-shifted spectrum after radial velocity correction. The radial velocity value of the spectrum is given in the upper left area of the diagram. The two yellow rectangular regions on the two sides of the diagram indicate the 20 \AA wide R and V pseudo-continuum bands. The two green triangular regions centered at 3969.59 \AA and 3934.78 \AA indicate the 1.09 \AA FWHM triangular bandpasses for Ca II H line and K line, respectively. Within the triangular regions are the 1 \AA rectangular bandpasses which are shown in yellow. The stellar chromospheric activity parameters derived in this work are displayed in the area just above the spectrum plot. The obsid , FITS file name, data release number, and several stellar and spectroscopic parameters of the LAMOST spectrum are given in the title area of the diagram.

‘000/’, ‘001/’, etc.). The figure file of a certain spectrum diagram can be found through the path ‘ $\langle \text{first three digits of 9-digit-obsid} \rangle / \langle \text{figure file name of spectrum diagram} \rangle$ ’. For example, the figure file of the spectrum diagram displayed in Figure 9 is located at ‘054/CaIIHK_obsid-054904030_spec-56199-EG000313N173308V_1_sp04-030.jpg’. There are 585 folders in total. These folders of spectrum diagrams are archived into multiple compressed ZIP packages, with each ZIP package containing no more than 50 folders. The filenames of the ZIP files follow the convention such as ‘spectrum_diagrams_000-049.zip’ to show the range of the folders contained in the ZIP files. These ZIP packages of spectrum diagrams are available through the online version of the database.

6. RESULTS AND DISCUSSION

6.1. Triangular Bandpass versus Rectangular Bandpass of Ca II H and K Lines

In Section 4.3, the S_{tri} and S_{rec} indexes are introduced based on the triangular bandpass and the rectangular bandpass at Ca II H&K line cores, respectively. The S_L index is further introduced by multiplying S_{tri} by a scaling factor. Figure 10 depicts the correlations of S_{rec} vs. S_{tri} , S_{tri} vs. S_L , and S_{rec} vs. S_L based on the derived values of the activity indexes in the database.

As shown in Figure 10, there is a good consistency between the values of S_{rec} , S_{tri} , and S_L for the LRS spectra. A linear fitting for S_{rec} vs. S_{tri} gives

$$S_{\text{tri}} = 0.983 S_{\text{rec}} + 0.0075 \quad (14)$$

(see Figure 10a), which means that for larger values (> 0.456) of activity indexes, S_{rec} is generally slightly greater than S_{tri} . The relation between S_{tri} and S_L has been given by Equation (8) (also see Figure 10b). A linear fitting for

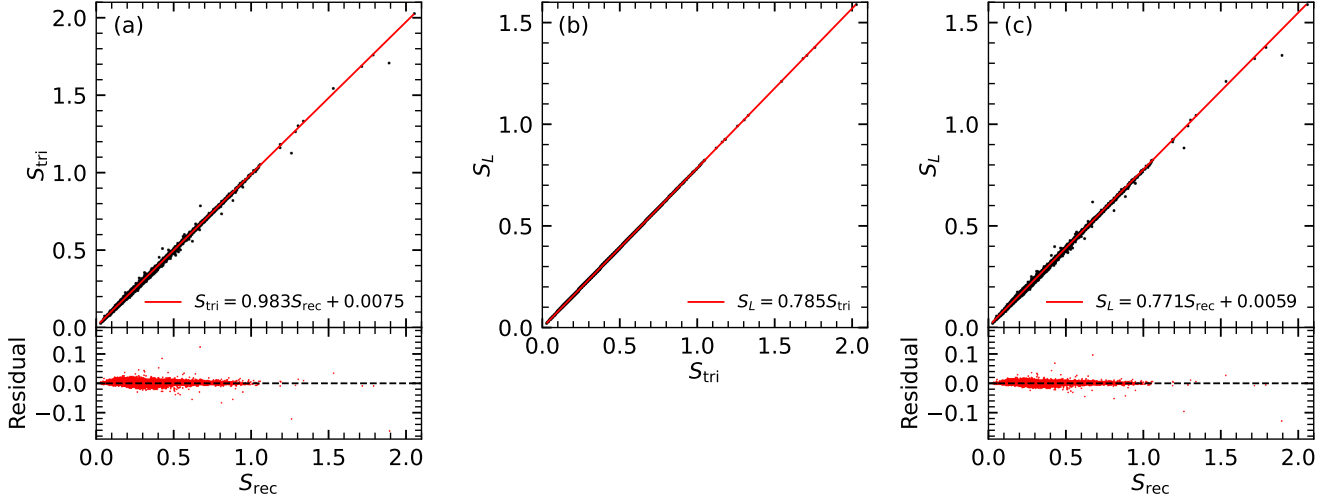


Figure 10. Scatter plots of (a) S_{rec} vs. S_{tri} , (b) S_{tri} vs. S_L , and (c) S_{rec} vs. S_L based on the values of the activity indexes in the database. The red lines are linear fittings to the correlations between the activity indexes. The formulas for the fitting results are given in the plots. The residuals of the fittings are also given for panels (a) and (c). There are no residuals in panel (b) since the relation between S_{tri} and S_L is directly defined by Equation (8).

S_{rec} vs. S_L gives

$$S_L = 0.771 S_{\text{rec}} + 0.0059 \quad (15)$$

(see Figure 10c). Note that Equation (15) can be deduced from Equations (8) and (14).

In comparison to the S_{tri} and S_L indexes defined based on the triangular bandpass at line cores of Ca II H&K lines, the S_{rec} index defined based on the rectangular bandpass has a more straightforward physical meaning and is also a reliable and suitable choice for stellar activity studies with the LRS spectra. The mean S_{MWO} index value of the Sun is about 0.169 as determined by Egeland et al. (2017) based on the MWO HKP-2 measurements. By substituting this value to Equation (6) and then using Equation (15), we can get the mean S_{rec} value of the Sun (denoted by $\langle S_{\text{rec}, \odot} \rangle$) is about 0.223.

6.2. Uncertainty of Activity Index versus SNR of Spectra

The uncertainty of the activity indexes is related to the SNR of spectra. A larger SNR usually corresponds to a smaller uncertainty of activity index. We utilize all the derived uncertainty values of S_{rec} in Section 4.4 and the SNR_g values of the LAMOST LRS spectra to quantitatively analyze this relation. (The analysis can also be performed for S_{tri} and S_L , and the results are similar.)

In Section 4.4, we have obtained the uncertainties of S_{rec} originating from the uncertainty of spectral flux, the discretization in spectral data, and the uncertainty of radial velocity (denoted by $\delta S_{\text{rec}, \text{flux}}$, $\delta S_{\text{rec}, \text{discrete}}$, and $\delta S_{\text{rec}, V_r}$, respectively), as well as the composite uncertainty of S_{rec} caused by all the three uncertainty sources (denoted by δS_{rec}). The scatter plots illustrating the distributions of $\log \text{SNR}_g$ vs. $\log \delta S_{\text{rec}, \text{flux}}$, $\log \text{SNR}_g$ vs. $\log \delta S_{\text{rec}, \text{discrete}}$, $\log \text{SNR}_g$ vs. $\log \delta S_{\text{rec}, V_r}$, and $\log \text{SNR}_g$ vs. $\log \delta S_{\text{rec}}$ are displayed in the left panels of Figure 11. We also calculate the corresponding relative uncertainties of S_{rec} (i.e., $\delta S_{\text{rec}, \text{flux}}/S_{\text{rec}}$, $\delta S_{\text{rec}, \text{discrete}}/S_{\text{rec}}$, $\delta S_{\text{rec}, V_r}/S_{\text{rec}}$, and $\delta S_{\text{rec}}/S_{\text{rec}}$), and the distributions of $\log \text{SNR}_g$ vs. $\log \delta S_{\text{rec}, \text{flux}}/S_{\text{rec}}$, $\log \text{SNR}_g$ vs. $\log \delta S_{\text{rec}, \text{discrete}}/S_{\text{rec}}$, $\log \text{SNR}_g$ vs. $\log \delta S_{\text{rec}, V_r}/S_{\text{rec}}$, and $\log \text{SNR}_g$ vs. $\log \delta S_{\text{rec}}/S_{\text{rec}}$ are displayed in the right panels of Figure 11.

It can be seen from Figure 11 that a power law relation is roughly satisfied between SNR_g and $\delta S_{\text{rec}, \text{flux}}$ as well as between SNR_g and $\delta S_{\text{rec}, \text{flux}}/S_{\text{rec}}$ (Figures 11a and b), however, the values of δS_{rec} and $\delta S_{\text{rec}}/S_{\text{rec}}$ are distributed over a relatively wide strip area. The order of magnitude of $\delta S_{\text{rec}, \text{discrete}}$ (Figures 11c and d) is generally smaller than $\delta S_{\text{rec}, \text{flux}}$, and the order of magnitude of $\delta S_{\text{rec}, V_r}$ (Figures 11e and f) in turn is generally smaller than $\delta S_{\text{rec}, \text{discrete}}$, which has been demonstrated in Figure 8.

Figures 11g and h show that the composite uncertainty δS_{rec} is mainly affected by $\delta S_{\text{rec}, \text{flux}}$ for smaller SNR_g values and by $\delta S_{\text{rec}, \text{discrete}}$ for larger SNR_g values. We performed cubic polynomial fitting for the upper envelope, mean value, and lower envelope of the distributions of $\log \delta S_{\text{rec}}$ and $\log \delta S_{\text{rec}}/S_{\text{rec}}$ in Figures 11g and h. We divide the range of $\log \text{SNR}_g$ (from $\log 50=1.7$ to $\log 1000=3.0$) into 300 equal-width bins and use the upper envelope, mean, and

lower envelope values of $\log \delta S_{\text{rec}}$ and $\log \delta S_{\text{rec}}/S_{\text{rec}}$ in each bin for fitting. The upper envelope and lower envelope threshold is defined as the number density value in Figures 11g and h no less than 5 in each bin. If all the number density values in a bin are less than 5, the bin does not participate in the fitting. The fitting results are illustrated in Figures 11g and h.

The formulas for the fitted upper envelope, mean value, and lower envelope of the $\log \delta S_{\text{rec}}$ distribution are given in Equations (16), (17), and (18), respectively, in which x represents $\log \text{SNR}_g$ and y represents $\log \delta S_{\text{rec}}$:

$$y = -0.041x^3 + 1.304x^2 - 6.389x + 6.288, \quad (16)$$

$$y = -0.157x^3 + 1.880x^2 - 6.806x + 5.415, \quad (17)$$

$$y = -0.010x^3 + 0.788x^2 - 3.917x + 2.584. \quad (18)$$

The formulas for the fitted upper envelope, mean value, and lower envelope of the $\log \delta S_{\text{rec}}/S_{\text{rec}}$ distribution are given in Equations (19), (20), and (21), respectively, in which x represents $\log \text{SNR}_g$ and y' represents $\log \delta S_{\text{rec}}/S_{\text{rec}}$:

$$y' = -0.231x^3 + 2.598x^2 - 9.317x + 9.133, \quad (19)$$

$$y' = -0.134x^3 + 1.703x^2 - 6.391x + 5.726, \quad (20)$$

$$y' = -0.152x^3 + 1.984x^2 - 7.063x + 5.738. \quad (21)$$

Equations (16)–(21) can be used to make a preliminary estimation of the values of δS_{rec} and $\delta S_{\text{rec}}/S_{\text{rec}}$ from the value of SNR_g . For example, by using Equation (20) (illustrated by the black dashed line in Figure 11h), it can be deduced that the mean value of $\log \delta S_{\text{rec}}/S_{\text{rec}}$ for $\text{SNR}_g = 50$ is about -0.87 and the corresponding $\delta S_{\text{rec}}/S_{\text{rec}}$ value is about $10^{-0.87} \approx 0.13$. By using Equation (16) (illustrated by the red line in Figure 11g), it can be deduced that the upper envelope value of $\log \delta S_{\text{rec}}$ for $\text{SNR}_g = 50$ is about -1.0 , which means the whole upper envelope line of $\log \delta S_{\text{rec}}$ is well below -1.0 and the corresponding δS_{rec} value is below $10^{-1.0} = 0.1$. Considering the distribution range of the S_{rec} values (about $10^0 = 1.0$; see Figures 12), it is appropriate to set the upper limit of the uncertainty values of S_{rec} to about $10^{-1} = 0.1$. This requirement leads to the SNR_g condition ($\text{SNR}_g \geq 50.00$) for selecting LRS spectra in Section 3.

6.3. Overall Distribution of Chromospheric Activity of Solar-like Stars

We use the full data set of the derived S_{rec} values in the database to show the overall distribution of chromospheric activity of solar-like stars. The distributions of S_{tri} and S_L are similar since they have approximate linear relations with S_{rec} (see Figures 10a and c).

The histogram of all the S_{rec} values in the database is displayed in Figure 12. Figure 12a uses a linear scale for vertical axis and Figure 12b a logarithmic scale. As shown in Figure 12a, most of the spectra in the database are associated with stars that are not very active with the values of S_{rec} distributed around the mean S_{rec} value of the Sun ($\langle S_{\text{rec}, \odot} \rangle = 0.223$; see Section 6.1). Figure 12b demonstrates that there are a certain number of spectra having a higher value of S_{rec} which might be associated with active stars, and a dozen of spectra have isolated S_{rec} values greater than 1.1. The features of the spectra with higher values of S_{rec} will be examined in detail in the further work.

The relationship between the stellar activity and the stellar parameters (T_{eff} , $\log g$, and $[\text{Fe}/\text{H}]$) has attracted wide interest in the literature (e.g., Wilson 1968; Gray et al. 2006; Mittag et al. 2013; Zhao et al. 2013, 2015; Lorenzo-Oliveira et al. 2016; Boro Saikia et al. 2018; Fang et al. 2018; Karoff et al. 2018; Zhang et al. 2019; Gomes da Silva et al. 2021). In Figure 13, we display the scatter diagrams of T_{eff} vs. S_{rec} , $\log g$ vs. S_{rec} , and $[\text{Fe}/\text{H}]$ vs. S_{rec} using the values of the stellar parameters and activity indexes in the database, with color scale indicating number density.

In Figure 14, we display the distribution of S_{rec} values in scatter diagrams of T_{eff} vs. $\log g$, T_{eff} vs. $[\text{Fe}/\text{H}]$, and $[\text{Fe}/\text{H}]$ vs. $\log g$, with color scale indicating the value of S_{rec} (see the color bar in Figure 14). The smaller S_{rec} values (< 0.4) are displayed in blue, the medium S_{rec} values (0.4–0.6) are green, and the larger S_{rec} values (> 0.6) are red. The data points in Figure 14 are drawn in order from smallest S_{rec} at the bottom to largest at the top, and hence the data points with larger S_{rec} values are overlaid on top of the data points with smaller S_{rec} values. As shown in Figure 14, most of the spectra have lower S_{rec} values (blue color). The higher the S_{rec} value, the smaller the distribution range is.

From the distribution diagrams of S_{rec} with respect to $\log g$ and $[\text{Fe}/\text{H}]$ (Figures 13b and c), it can be seen that the distribution morphology of the sample with $S_{\text{rec}} > 6.0$ is different from the sample with $S_{\text{rec}} < 6.0$. That is, the

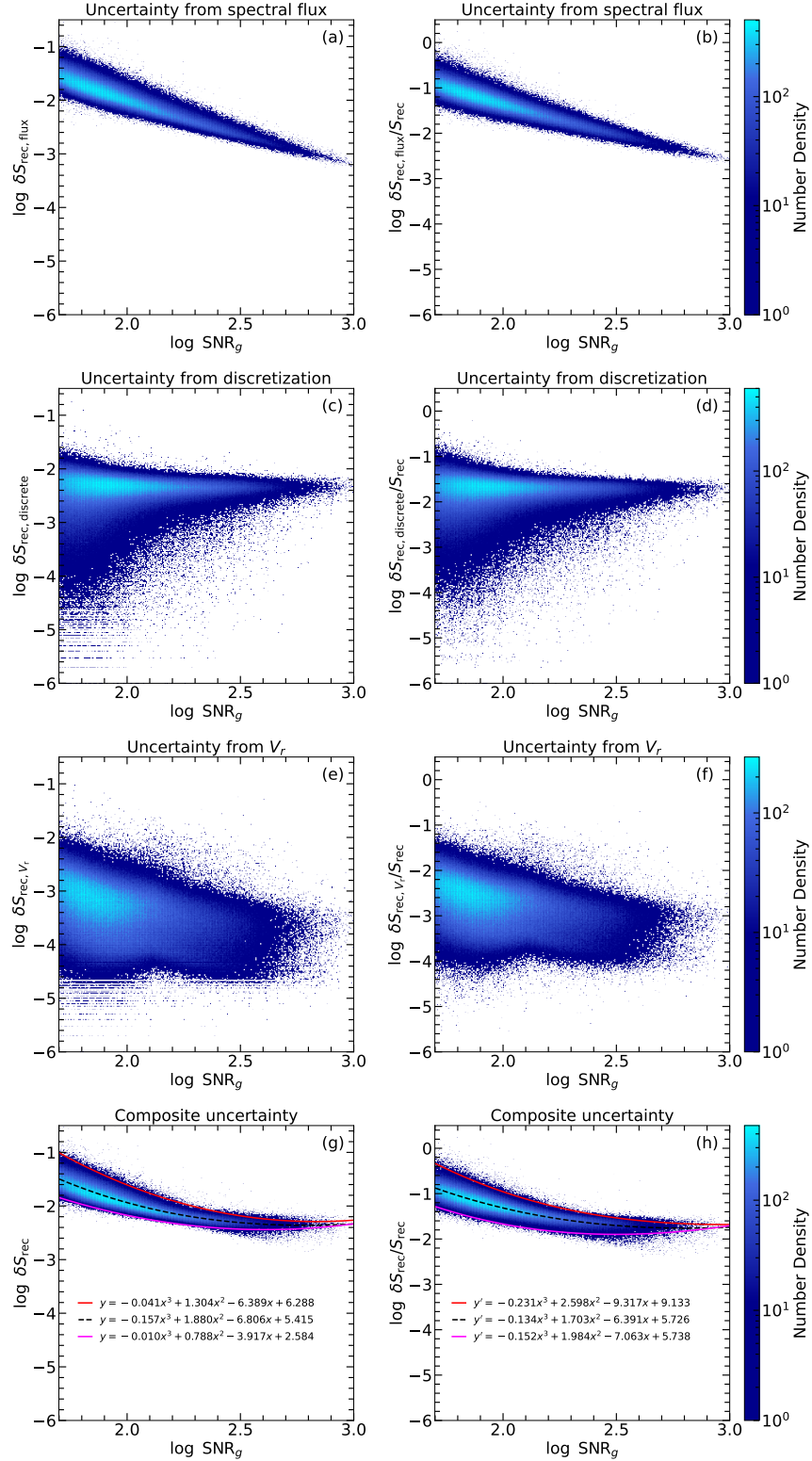


Figure 11. Distributions of $\log \text{SNR}_g$ vs. (a) $\log \delta S_{\text{rec, flux}}$, (b) $\log \delta S_{\text{rec, flux}}/S_{\text{rec}}$, (c) $\log \delta S_{\text{rec, discrete}}$, (d) $\log \delta S_{\text{rec, discrete}}/S_{\text{rec}}$, (e) $\log \delta S_{\text{rec, } V_r}$, (f) $\log \delta S_{\text{rec, } V_r}/S_{\text{rec}}$, (g) $\log \delta S_{\text{rec}}$, and (h) $\log \delta S_{\text{rec}}/S_{\text{rec}}$. The color scale represents number density. In panels g and h, the cubic polynomial fitting lines for upper envelope, mean value, and lower envelope of the distributions are plotted with red, black dashed, and violet lines, respectively. The formulas for the fitted lines are also displayed, with x representing $\log \text{SNR}_g$, y representing $\log \delta S_{\text{rec}}$, and y' representing $\log \delta S_{\text{rec}}/S_{\text{rec}}$.

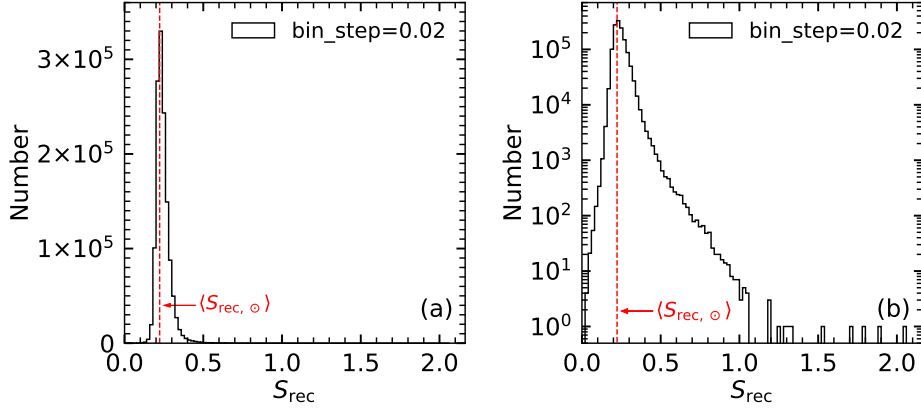


Figure 12. Histograms of the S_{rec} values of solar-like stars in the database with vertical axis (a) in linear scale and (b) in logarithmic scale. The mean S_{rec} value of the Sun ($\langle S_{\text{rec}, \odot} \rangle = 0.223$) is indicated by a vertical dashed line in the plots.

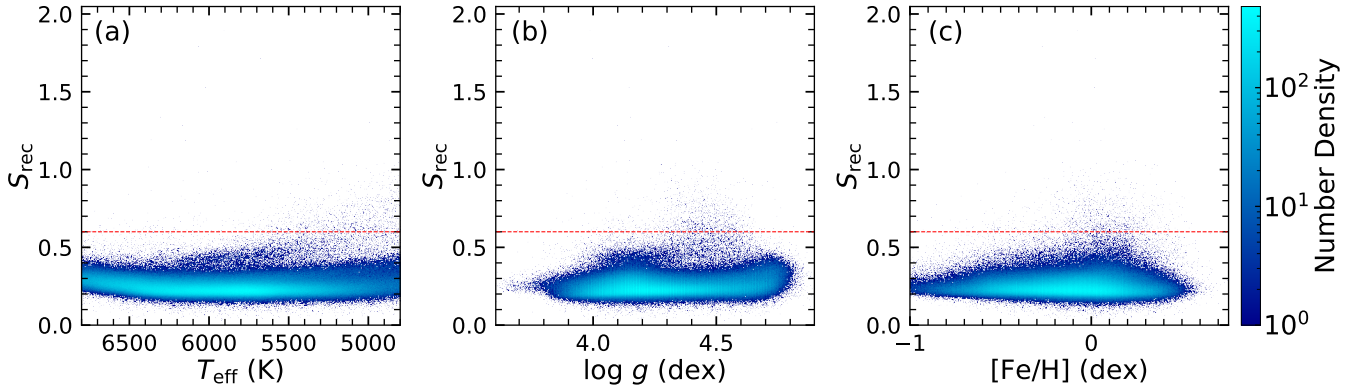


Figure 13. Scatter diagrams of (a) T_{eff} vs. S_{rec} , (b) $\log g$ vs. S_{rec} , and (c) $[\text{Fe}/\text{H}]$ vs. S_{rec} for all the LAMOST LRS spectra of solar-like stars in the database. Color scale indicates number density. The horizontal dashed lines indicate $S_{\text{rec}} = 0.6$; the sample above the line tends to appear in a compact range of $\log g$ (in panel b) and $[\text{Fe}/\text{H}]$ (in panel c).

sample with $S_{\text{rec}} > 0.6$ tends to appear in a compact range of stellar parameters. We draw a horizontal line indicating $S_{\text{rec}} = 0.6$ in Figures 13 to distinguish between the two regions with different morphologies of distribution. The total number of the spectra with S_{rec} greater than 0.6 is 1424, which is about 0.1% of the total spectra in the database. Compared to previous investigations on the stellar chromospheric activity index distribution with respect to surface gravity and metallicity in the literature (e.g., Gray et al. 2006; Jenkins et al. 2008; Lovis et al. 2011; Zhao et al. 2013; Karoff et al. 2018), this feature of the S_{rec} distribution can be revealed thanks to the huge amounts of spectral data obtained by LAMOST. With the assistance of Figure 14, it can be determined that the stars with S_{rec} greater than 0.6 tend to appear in the parameter range of $T_{\text{eff}} < 5500$ K, $4.3 < \log g < 4.6$, and $-0.2 < [\text{Fe}/\text{H}] < 0.3$.

It should be noted that the S_{rec} as well as other S -index parameters (e.g., S_{tri} and S_L in this work) is temperature (color) dependent by construction (e.g., Wilson 1968), as demonstrated by the curved baseline in Figure 13a. The color-corrected indexes such as R'_{HK} (Linsky et al. 1979; Noyes et al. 1984a) will be introduced for the LAMOST LRS spectra of solar-like stars in our future work.

7. SUMMARY AND CONCLUSION

We obtain 1,330,654 high-quality LRS spectra of solar-like stars from LAMOST DR7. The emission fluxes of Ca II H&K line cores are measured by employing 1 \AA rectangular bandpasses as well as 1.09 \AA FWHM triangular bandpasses. The emission fluxes of pseudo-continuum on the two sides of the Ca II H&K lines are measured by using 20 \AA rectangular bandpasses. We introduce three activity indexes S_{tri} , S_L , and S_{rec} of Ca II H&K lines, and calculate the values of the activity indexes for all the obtained LRS spectra of solar-like stars. By examining the relations of the three indexes, we suggest that for the LAMOST LRS data, the S_{rec} index using rectangular bandpass is also a reliable

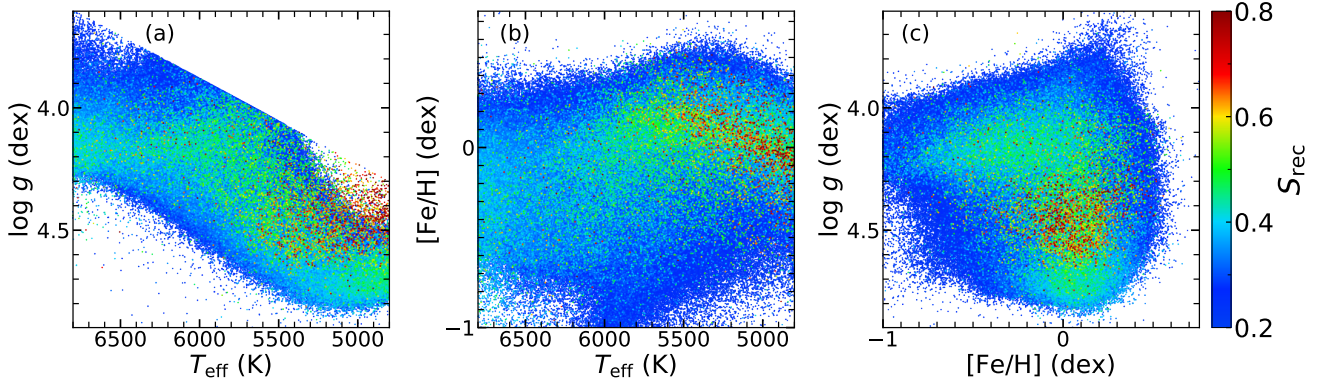


Figure 14. Distribution of S_{rec} values in scatter diagrams of (a) T_{eff} vs. $\log g$, (b) T_{eff} vs. $[\text{Fe}/\text{H}]$, and (c) $[\text{Fe}/\text{H}]$ vs. $\log g$ for all the LAMOST LRS spectra of solar-like stars in the database. The value of S_{rec} is indicated by color scale. The data points with larger S_{rec} are overlaid on top of the data points with smaller S_{rec} .

indicator of chromospheric activity with a more straightforward physical meaning than the indexes using triangular bandpass. Through the analysis of the S_{rec} distribution with stellar parameters, it is found that the solar-like stars with high level of chromospheric activity ($S_{\text{rec}} > 0.6$) tend to appear in the stellar parameter range of $T_{\text{eff}} < 5500$ K, $4.3 < \log g < 4.6$, and $-0.2 < [\text{Fe}/\text{H}] < 0.3$.

A stellar chromospheric activity database of solar-like stars is constructed from all the 1,330,654 LAMOST LRS spectra obtained in this work. The database is composed of a catalog of spectral sample and activity parameters and a library of spectrum diagrams of Ca II H&K lines. The catalog of the database provides the six derived emission flux measures of Ca II H&K lines (\tilde{R} , \tilde{V} , \tilde{H}_{tri} , \tilde{K}_{tri} , \tilde{H}_{rec} , and \tilde{K}_{rec}), the three stellar chromospheric activity indexes (S_{tri} , S_L , and S_{rec}), and their uncertainties for all the LRS spectra employed by the database. The library of spectrum diagrams provide 1,330,654 spectral profile pictures of Ca II H&K lines for the spectral sample in the database, in which the chromospheric activity parameters as well as the spectroscopic parameters are displayed. All the components of the database are available online (see Section 5).

Based on the database, one can investigate overall chromospheric activity properties of solar-like stars (such as the relation of activity index with stellar parameters, age, rotation period, etc.) and understand solar-stellar connection through chromospheric activity (He et al. 2021). We have shown the relationship between S_{rec} and stellar parameters T_{eff} , $\log g$, and $[\text{Fe}/\text{H}]$ in this work. It is also important to investigate the connections of the stellar chromospheric activity revealed by the LAMOST spectral data with the stellar photospheric activity indicated by rotational modulation in the light curve data observed by Kepler/K2, TESS, etc. (e.g., He et al. 2015, 2018; Mehrabi et al. 2017; Mehrabi & He 2019; Reinhold et al. 2020; Zhang et al. 2020a,b), the stellar coronal activity revealed by the X-ray data observed by Chandra, XMM-Newton, etc. (e.g., He et al. 2019; Wang et al. 2020), and the stellar flare activity revealed by stellar light curve data and spectral data (e.g., Maehara et al. 2012; He et al. 2018; Li et al. 2018; Goodarzi et al. 2019, 2021; Yan et al. 2021; Wu et al. 2022). The time-domain data of LAMOST have been released (e.g., Liu et al. 2020; Zong et al. 2020; Bai et al. 2021; Wang et al. 2021), and the method developed in this work can be used for time-domain analysis of stellar chromospheric activity. Stellar chromospheric activity information is also usefully for exploring habitability of exoplanet as well as exoplanet detection (e.g., Saar & Donahue 1997; Isaacson & Fischer 2010; Lovis et al. 2011; Gomes da Silva et al. 2021).

ACKNOWLEDGEMENTS

This work is supported by the National Key R&D Program of China (2019YFA0405000) and the National Natural Science Foundation of China (12073001 and 11973059). W.Z. and J.Z. thank the support of the Anhui Project (Z010118169). H.H. acknowledges the B-type Strategic Priority Program of the Chinese Academy of Sciences (XDB41000000), the CAS Strategic Pioneer Program on Space Science (XDA15052200), and the Astronomical Big Data Joint Research Center, co-founded by the National Astronomical Observatories, Chinese Academy of Sciences (NAOC) and the Alibaba Cloud. Guoshoujing Telescope (the Large Sky Area Multi-Object Fiber Spectroscopic Telescope, LAMOST) is a National Major Scientific Project built by the Chinese Academy of Sciences. Funding for the

project has been provided by the National Development and Reform Commission. LAMOST is operated and managed by the National Astronomical Observatories, Chinese Academy of Sciences.

Facility: LAMOST

Software: Astropy (Astropy Collaboration et al. 2013, 2018), SciPy (Virtanen et al. 2020), NumPy (Oliphant 2007; van der Walt et al. 2011; Harris et al. 2020), Matplotlib (Hunter 2007)

APPENDIX

A. CALIBRATION PROCEDURE FOR THE RELATIONSHIP BETWEEN S_L AND S_{MWO}

We identify 65 common stars between the selected LRS spectra of solar-like stars in this work and the S_{MWO} catalog of MWO given by Duncan et al. (1991). We do not find common stars with the MWO catalog by Baliunas et al. (1995). These common stars are listed in Table 4 and used for S_L and S_{MWO} relationship calibration. The S_{MWO} values in Table 4 are taken from Duncan et al. (1991), and the S_L values are taken from the catalog obtained by this work. If a stellar object has more than one S -index records in a catalog, the median of the S -index records is adopted.

To determine the parameters of the exponential relation between S_L and S_{MWO} shown in Equation (6), we perform a linear fitting for the values of S_L and $\ln S_{MWO}$ of the common stars, as illustrated in Figure 15. The original data of S_L and $\ln S_{MWO}$ of the common stars are displayed as black dots in Figure 15. It can be seen from Figure 15 that the values of $\ln S_{MWO}$ of the common stars are not evenly distributed in the Y-axis direction. To obtain a relatively evenly distributed data set, we divide the distribution range of the $\ln S_{MWO}$ values (from -2 to 0) into 20 equal bins (bin step = 0.1) as illustrated in Figure 15, and combine the data points in each bin into one data point which is displayed as a red dot in each bin in Figure 15. The Y-coordinate of the combined data point in a bin is the center position of the bin in Y-axis, and the X-coordinate of the combined data point is the median of the S_L values of the original data points within the bin. The linear fitting is performed for the red dots in Figure 15, and the fitting result is displayed as a black line. The formula for the fitted line is

$$\ln S_{MWO} = 8.806 S_L - 3.348. \quad (\text{A1})$$

Then, the exponential relation between S_L and S_{MWO} in Equation (6) can be derived from Equation (A1).

Table 4. Common Stars Used for S_L and S_{MWO} Relationship Calibration.

Star Name	S_L	δS_L	S_{MWO}	δS_{MWO}	Gaia DR2 Source Identifier
BD +58 1199	0.174	0.0089	0.198	0.0297	Gaia DR2 1025549786973693312
Cl Melotte 25 42	0.242	0.0033	0.314	0.0084	Gaia DR2 145325548516513280
HD 118576	0.179	0.0042	0.165	0.0030	Gaia DR2 1456026937348507520
HD 7983	0.187	0.0031	0.202		Gaia DR2 2471972451598042880
HD 1342	0.198	0.0032	0.173	0.0033	Gaia DR2 2547169391852546688
Parenago 1199	0.176	0.0033	0.365		Gaia DR2 3017234389666905216
Parenago 1626	0.348	0.0045	0.584		Gaia DR2 3017237653842191616
Parenago 1158	0.202	0.0034	0.375		Gaia DR2 3209419916870340992
Parenago 1361	0.225	0.0035	0.409		Gaia DR2 3209536636903447936
Parenago 1241	0.290	0.0022	0.407		Gaia DR2 3209543989887451776
Parenago 1322	0.433	0.0066	0.902		Gaia DR2 3209604390008665216

Table 4 continued on next page

Table 4 (*continued*)

Star Name	S_L	δS_L	S_{MWO}	δS_{MWO}	Gaia DR2 Source Identifier
Parenago 1357	0.186	0.0046	0.298		Gaia DR2 3209656071350169344
BD +00 0873	0.169	0.0042	0.147		Gaia DR2 3231423476711449728
Cl Melotte 25 99	0.280	0.0010	0.541	0.0273	Gaia DR2 3309956850635519488
Cl Melotte 25 46	0.269	0.0011	0.239		Gaia DR2 3311148828615843328
Cl Melotte 25 25	0.297	0.0014	0.251		Gaia DR2 3312281669189449472
Cl Melotte 25 79	0.250	0.0012	0.447	0.0353	Gaia DR2 3314213025787054592
Cl Melotte 111 150	0.384	0.0028	0.552		Gaia DR2 3960008298439044864
Cl Melotte 111 92	0.238	0.0051	0.301		Gaia DR2 4008342623437661568
Cl Melotte 111 97	0.240	0.0051	0.298		Gaia DR2 4008433608024885632
Cl Melotte 111 85	0.225	0.0039	0.287		Gaia DR2 4008706733584941312
Cl Melotte 111 132	0.245	0.0065	0.287		Gaia DR2 4008867674599508992
Cl Melotte 111 118	0.206	0.0042	0.231		Gaia DR2 4009051048227419520
Cl Melotte 111 86	0.233	0.0068	0.245		Gaia DR2 4009518100151157248
Cl Melotte 25 7	0.301	0.0000	0.220		Gaia DR2 43538293935879680
HD 149162	0.220	0.0046	0.213	0.0252	Gaia DR2 4433380077474648192
Cl Melotte 25 69	0.242	0.0019	0.401	0.0464	Gaia DR2 48061409893621248
Cl Melotte 25 43	0.280	0.0021	0.357		Gaia DR2 48197783694869760
Cl Melotte 25 5	0.300	0.0047	0.421	0.0076	Gaia DR2 64266768177592448
Cl Melotte 22 2106	0.307	0.0049	0.739		Gaia DR2 64921458633614976
Cl Melotte 22 2126	0.301	0.0058	0.822		Gaia DR2 64923279699744256
Cl Melotte 22 2345	0.292	0.0040	0.316	0.0028	Gaia DR2 64930495244783616
Cl Melotte 22 1139	0.219	0.0035	0.224		Gaia DR2 64952829074688896
Cl Melotte 22 923	0.253	0.0021	0.452		Gaia DR2 64971177174850304
Cl Melotte 22 1797	0.267	0.0071	0.347		Gaia DR2 64999588381514496
Cl Melotte 22 1215	0.248	0.0021	0.429		Gaia DR2 65004712279475712
Cl Melotte 22 1613	0.225	0.0028	0.308		Gaia DR2 65020414679879296
Cl Melotte 22 164	0.287	0.0070	0.327		Gaia DR2 65090680344356992
Cl Melotte 22 1117	0.254	0.0021	0.285		Gaia DR2 65199978672758272
Cl Melotte 22 708	0.281	0.0024	0.346		Gaia DR2 65222759179189248
Cl Melotte 22 1122	0.237	0.0035	0.281		Gaia DR2 65225611037551360
Cl Melotte 22 129	0.263	0.0033	0.525		Gaia DR2 65233788655261568
Cl Melotte 22 233	0.211	0.0039	0.191		Gaia DR2 65242069352190976
Cl Melotte 22 745	0.256	0.0032	0.277		Gaia DR2 65277975278721152
Cl Melotte 22 489	0.272	0.0051	0.374		Gaia DR2 65295425728422528
Cl* NGC 2632 KW 162	0.228	0.0032	0.310		Gaia DR2 661207024061875456
Cl* NGC 2632 KW 301	0.224	0.0037	0.410		Gaia DR2 661212933936844416
Cl* NGC 2632 KW 217	0.243	0.0050	0.276		Gaia DR2 661216743570426240
Cl* NGC 2632 KW 250	0.209	0.0051	0.216		Gaia DR2 661298451027341056
Cl* NGC 2632 KW 246	0.247	0.0092	0.776		Gaia DR2 661310923612365312
Cl* NGC 2632 KW 238	0.261	0.0000	0.365		Gaia DR2 661311752544249088
Cl* NGC 2632 KW 32	0.262	0.0000	0.384		Gaia DR2 664283079638402688

Table 4 *continued on next page*

Table 4 (*continued*)

Star Name	S_L	δS_L	S_{MWO}	δS_{MWO}	Gaia DR2 Source Identifier
Cl* NGC 2632 KW 58	0.243	0.0028	0.442		Gaia DR2 664311392062657920
Cl* NGC 2632 KW 127	0.211	0.0027	0.257		Gaia DR2 664324684984105728
Cl Melotte 22 2147	0.455	0.0035	0.796		Gaia DR2 66503449709270400
Cl Melotte 22 1856	0.229	0.0025	0.320		Gaia DR2 66523893753437824
Cl Melotte 22 2027	0.279	0.0042	0.257		Gaia DR2 66720946851771904
Cl Melotte 22 1309	0.268	0.0034	0.359		Gaia DR2 66729261908482048
Cl Melotte 22 996	0.254	0.0026	0.439	0.0120	Gaia DR2 66788291938818304
Cl Melotte 22 727	0.298	0.0072	0.408		Gaia DR2 66802654309459712
Cl Melotte 22 1207	0.281	0.0029	0.451		Gaia DR2 66809491897360896
Cl Melotte 25 4	0.263	0.0000	0.303	0.0414	Gaia DR2 68001499939741440
Cl Melotte 22 25	0.233	0.0035	0.224		Gaia DR2 68310561489710336
Cl Melotte 22 405	0.258	0.0024	0.328	0.0332	Gaia DR2 69811948914407168
Cl Melotte 22 605	0.231	0.0049	0.260		Gaia DR2 69819404977607168

NOTE—The S_{MWO} values of MWO are taken from Duncan et al. (1991). The star names are taken from the online catalog of the MWO data (<https://cdsarc.cds.unistra.fr/viz-bin/cat/III/159A>). The Gaia DR2 Source Identifiers are taken from the LAMOST LRS AFGK Catalog. The S_L values are taken from the catalog obtained by this work. If a stellar object has more than one S -index records in a catalog, the median of the S -index records is adopted. Some of the uncertainty values are blank because they are not available in the source catalog.

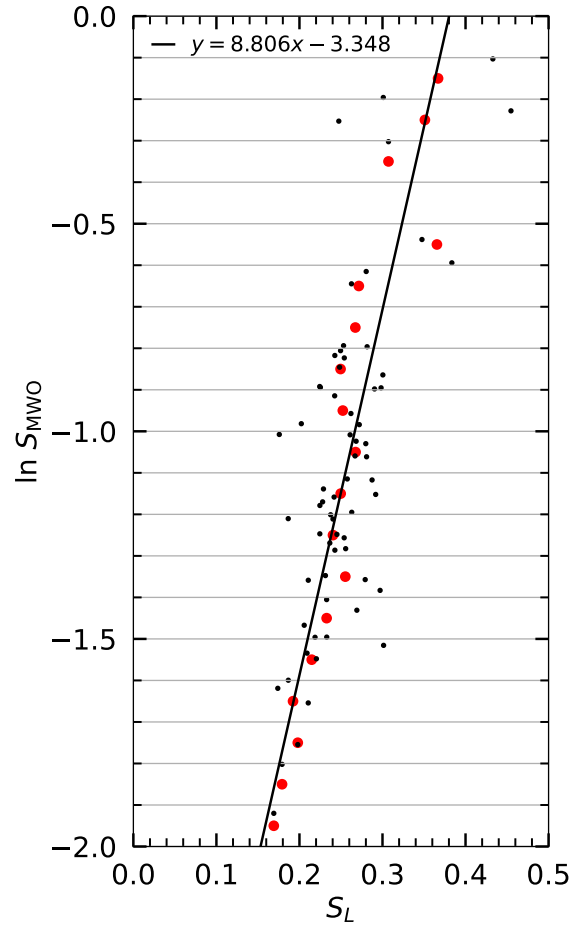


Figure 15. Linear fitting for the values of S_L and $\ln S_{MWO}$ of the common stars. Black dots are the original data as listed in Table 4. The values of $\ln S_{MWO}$ of the common stars are distributed in the range from -2 to 0 , which is divided into 20 equal bins (bin step = 0.1) distinguished by horizontal lines. The red dots indicate the median of the S_L values in each bin. The linear fitting is performed for the red dots in the plot, and the fitting result is displayed as a black line. The formula for the fitted line is displayed, with x representing S_L and y representing $\ln S_{MWO}$.

REFERENCES

- Astropy Collaboration, Robitaille, T. P., Tollerud, E. J., et al. 2013, *A&A*, 558, A33, doi: [10.1051/0004-6361/201322068](https://doi.org/10.1051/0004-6361/201322068)
- Astropy Collaboration, Price-Whelan, A. M., Sipőcz, B. M., et al. 2018, *AJ*, 156, 123, doi: [10.3847/1538-3881/aabc4f](https://doi.org/10.3847/1538-3881/aabc4f)
- Bai, Z.-R., Zhang, H.-T., Yuan, H.-L., et al. 2021, *Research in Astronomy and Astrophysics*, 21, 249, doi: [10.1088/1674-4527/21/10/249](https://doi.org/10.1088/1674-4527/21/10/249)
- Baliunas, S., & Jastrow, R. 1990, *Nature*, 348, 520, doi: [10.1038/348520a0](https://doi.org/10.1038/348520a0)
- Baliunas, S. L., Donahue, R. A., Soon, W. H., et al. 1995, *ApJ*, 438, 269, doi: [10.1086/175072](https://doi.org/10.1086/175072)
- Beck, P. G., Allende Prieto, C., Van Reeth, T., et al. 2016, *A&A*, 589, A27, doi: [10.1051/0004-6361/201425423](https://doi.org/10.1051/0004-6361/201425423)
- Boro Saikia, S., Marvin, C. J., Jeffers, S. V., et al. 2018, *A&A*, 616, A108, doi: [10.1051/0004-6361/201629518](https://doi.org/10.1051/0004-6361/201629518)
- Cayrel de Strobel, G. 1996, *A&A Rv*, 7, 243, doi: [10.1007/s001590050006](https://doi.org/10.1007/s001590050006)
- Choudhuri, A. R. 2017, *Science China Physics, Mechanics & Astronomy*, 60, 019601, doi: [10.1007/s11433-016-0413-7](https://doi.org/10.1007/s11433-016-0413-7)
- Ciddor, P. E. 1996, *ApOpt*, 35, 1566, doi: [10.1364/AO.35.001566](https://doi.org/10.1364/AO.35.001566)
- Cui, X.-Q., Zhao, Y.-H., Chu, Y.-Q., et al. 2012, *Research in Astronomy and Astrophysics*, 12, 1197, doi: [10.1088/1674-4527/12/9/003](https://doi.org/10.1088/1674-4527/12/9/003)
- De Cat, P., Fu, J. N., Ren, A. B., et al. 2015, *ApJS*, 220, 19, doi: [10.1088/0067-0049/220/1/19](https://doi.org/10.1088/0067-0049/220/1/19)
- Delfosse, X., Forveille, T., Perrier, C., & Mayor, M. 1998, *A&A*, 331, 581
- Doi, M., Tanaka, M., Fukugita, M., et al. 2010, *AJ*, 139, 1628, doi: [10.1088/0004-6256/139/4/1628](https://doi.org/10.1088/0004-6256/139/4/1628)

- Duncan, D. K., Vaughan, A. H., Wilson, O. C., et al. 1991, *ApJS*, 76, 383, doi: [10.1086/191572](https://doi.org/10.1086/191572)
- Eberhard, G., & Schwarzschild, K. 1913, *ApJ*, 38, 292, doi: [10.1086/142037](https://doi.org/10.1086/142037)
- Egeland, R., Soon, W., Baliunas, S., et al. 2017, *ApJ*, 835, 25, doi: [10.3847/1538-4357/835/1/25](https://doi.org/10.3847/1538-4357/835/1/25)
- Fang, X.-S., Zhao, G., Zhao, J.-K., & Bharat Kumar, Y. 2018, *MNRAS*, 476, 908, doi: [10.1093/mnras/sty212](https://doi.org/10.1093/mnras/sty212)
- Frasca, A., Molenda-Żakowicz, J., De Cat, P., et al. 2016, *A&A*, 594, A39, doi: [10.1051/0004-6361/201628337](https://doi.org/10.1051/0004-6361/201628337)
- Frebel, A., & Norris, J. E. 2015, *ARA&A*, 53, 631, doi: [10.1146/annurev-astro-082214-122423](https://doi.org/10.1146/annurev-astro-082214-122423)
- Fu, J.-N., Cat, P. D., Zong, W., et al. 2020, *Research in Astronomy and Astrophysics*, 20, 167, doi: [10.1088/1674-4527/20/10/167](https://doi.org/10.1088/1674-4527/20/10/167)
- Gaia Collaboration, Brown, A. G. A., Vallenari, A., et al. 2018, *A&A*, 616, A1, doi: [10.1051/0004-6361/201833051](https://doi.org/10.1051/0004-6361/201833051)
- Gomes da Silva, J., Santos, N. C., Adibekyan, V., et al. 2021, *A&A*, 646, A77, doi: [10.1051/0004-6361/202039765](https://doi.org/10.1051/0004-6361/202039765)
- Goodarzi, H., Mehrabi, A., Khosroshahi, H. G., & He, H. 2019, *ApJS*, 244, 37, doi: [10.3847/1538-4365/ab44cd](https://doi.org/10.3847/1538-4365/ab44cd)
- . 2021, *ApJ*, 906, 40, doi: [10.3847/1538-4357/abc8ea](https://doi.org/10.3847/1538-4357/abc8ea)
- Gray, R. O., Corbally, C. J., Garrison, R. F., et al. 2006, *AJ*, 132, 161, doi: [10.1086/504637](https://doi.org/10.1086/504637)
- Güdel, M. 2007, *Living Reviews in Solar Physics*, 4, 3, doi: [10.12942/lrsp-2007-3](https://doi.org/10.12942/lrsp-2007-3)
- Hale, G. E. 1908, *ApJ*, 28, 315, doi: [10.1086/141602](https://doi.org/10.1086/141602)
- Hall, J. C. 2008, *Living Reviews in Solar Physics*, 5, 2, doi: [10.12942/lrsp-2008-2](https://doi.org/10.12942/lrsp-2008-2)
- Hall, J. C., Henry, G. W., Lockwood, G. W., Skiff, B. A., & Saar, S. H. 2009, *AJ*, 138, 312, doi: [10.1088/0004-6256/138/1/312](https://doi.org/10.1088/0004-6256/138/1/312)
- Hall, J. C., Lockwood, G. W., & Skiff, B. A. 2007, *AJ*, 133, 862, doi: [10.1086/510356](https://doi.org/10.1086/510356)
- Harris, C. R., Millman, K. J., van der Walt, S. J., et al. 2020, *Nature*, 585, 357, doi: [10.1038/s41586-020-2649-2](https://doi.org/10.1038/s41586-020-2649-2)
- He, H., Wang, H., & Yun, D. 2015, *ApJS*, 221, 18, doi: [10.1088/0067-0049/221/1/18](https://doi.org/10.1088/0067-0049/221/1/18)
- He, H., Wang, H., Zhang, M., et al. 2018, *ApJS*, 236, 7, doi: [10.3847/1538-4365/aab779](https://doi.org/10.3847/1538-4365/aab779)
- He, H., Zhang, H., Wang, S., Yang, S., & Zhang, J. 2021, *Research Notes of the AAS*, 5, 6, doi: [10.3847/2515-5172/abd93b](https://doi.org/10.3847/2515-5172/abd93b)
- He, L., Wang, S., Liu, J., et al. 2019, *ApJ*, 871, 193, doi: [10.3847/1538-4357/aaf8b7](https://doi.org/10.3847/1538-4357/aaf8b7)
- Henry, T. J., Soderblom, D. R., Donahue, R. A., & Baliunas, S. L. 1996, *AJ*, 111, 439, doi: [10.1086/117796](https://doi.org/10.1086/117796)
- Hunter, J. D. 2007, *Computing in Science & Engineering*, 9, 90, doi: [10.1109/MCSE.2007.55](https://doi.org/10.1109/MCSE.2007.55)
- Isaacson, H., & Fischer, D. 2010, *ApJ*, 725, 875, doi: [10.1088/0004-637X/725/1/875](https://doi.org/10.1088/0004-637X/725/1/875)
- Jenkins, J. S., Jones, H. R. A., Pavlenko, Y., et al. 2008, *A&A*, 485, 571, doi: [10.1051/0004-6361:20078611](https://doi.org/10.1051/0004-6361:20078611)
- Jenkins, J. S., Murgas, F., Rojo, P., et al. 2011, *A&A*, 531, A8, doi: [10.1051/0004-6361/201016333](https://doi.org/10.1051/0004-6361/201016333)
- Karoff, C., Metcalfe, T. S., Montet, B. T., et al. 2019, *MNRAS*, 485, 5096, doi: [10.1093/mnras/stz782](https://doi.org/10.1093/mnras/stz782)
- Karoff, C., Knudsen, M. F., De Cat, P., et al. 2016, *Nature Communications*, 7, 11058, doi: [10.1038/ncomms11058](https://doi.org/10.1038/ncomms11058)
- Karoff, C., Metcalfe, T. S., Santos, Â. R. G., et al. 2018, *ApJ*, 852, 46, doi: [10.3847/1538-4357/aaa026](https://doi.org/10.3847/1538-4357/aaa026)
- Kesseli, A. Y., West, A. A., Veyette, M., et al. 2017, *ApJS*, 230, 16, doi: [10.3847/1538-4365/aa656d](https://doi.org/10.3847/1538-4365/aa656d)
- Li, C., Zhong, S. J., Xu, Z. G., et al. 2018, *MNRAS*, 479, L139, doi: [10.1093/mnrasl/sly117](https://doi.org/10.1093/mnrasl/sly117)
- Linsky, J. L. 2017, *ARA&A*, 55, 159, doi: [10.1146/annurev-astro-091916-055327](https://doi.org/10.1146/annurev-astro-091916-055327)
- Linsky, J. L., & Avrett, E. H. 1970, *PASP*, 82, 169, doi: [10.1086/128904](https://doi.org/10.1086/128904)
- Linsky, J. L., Worden, S. P., McClintock, W., & Robertson, R. M. 1979, *ApJS*, 41, 47, doi: [10.1086/190607](https://doi.org/10.1086/190607)
- Liu, C., Fu, J., Shi, J., et al. 2020, arXiv e-prints, arXiv:2005.07210. <https://arxiv.org/abs/2005.07210>
- Lorenzo-Oliveira, D., Porto de Mello, G. F., Dutra-Ferreira, L., & Ribas, I. 2016, *A&A*, 595, A11, doi: [10.1051/0004-6361/201628825](https://doi.org/10.1051/0004-6361/201628825)
- Lorenzo-Oliveira, D., Freitas, F. C., Meléndez, J., et al. 2018, *A&A*, 619, A73, doi: [10.1051/0004-6361/201629294](https://doi.org/10.1051/0004-6361/201629294)
- Lovis, C., Dumusque, X., Santos, N. C., et al. 2011, arXiv e-prints, arXiv:1107.5325. <https://arxiv.org/abs/1107.5325>
- Luo, A. L., Zhang, H.-T., Zhao, Y.-H., et al. 2012, *Research in Astronomy and Astrophysics*, 12, 1243, doi: [10.1088/1674-4527/12/9/004](https://doi.org/10.1088/1674-4527/12/9/004)
- Luo, A. L., Zhao, Y.-H., Zhao, G., et al. 2015, *Research in Astronomy and Astrophysics*, 15, 1095, doi: [10.1088/1674-4527/15/8/002](https://doi.org/10.1088/1674-4527/15/8/002)
- Maehara, H., Shibayama, T., Notsu, S., et al. 2012, *Nature*, 485, 478, doi: [10.1038/nature11063](https://doi.org/10.1038/nature11063)
- Mamajek, E. E., & Hillenbrand, L. A. 2008, *ApJ*, 687, 1264, doi: [10.1086/591785](https://doi.org/10.1086/591785)
- Mehrabi, A., & He, H. 2019, *NewA*, 66, 31, doi: [10.1016/j.newast.2018.07.007](https://doi.org/10.1016/j.newast.2018.07.007)
- Mehrabi, A., He, H., & Khosroshahi, H. 2017, *ApJ*, 834, 207, doi: [10.3847/1538-4357/834/2/207](https://doi.org/10.3847/1538-4357/834/2/207)
- Melbourne, K., Youngblood, A., France, K., et al. 2020, *AJ*, 160, 269, doi: [10.3847/1538-3881/abbf5c](https://doi.org/10.3847/1538-3881/abbf5c)
- Mittag, M., Schmitt, J. H. M. M., & Schröder, K. P. 2013, *A&A*, 549, A117, doi: [10.1051/0004-6361/201219868](https://doi.org/10.1051/0004-6361/201219868)

- Mittag, M., Schröder, K. P., Hempelmann, A., González-Pérez, J. N., & Schmitt, J. H. M. M. 2016, *A&A*, 591, A89, doi: [10.1051/0004-6361/201527542](https://doi.org/10.1051/0004-6361/201527542)
- Newton, E. R., Irwin, J., Charbonneau, D., et al. 2017, *ApJ*, 834, 85, doi: [10.3847/1538-4357/834/1/85](https://doi.org/10.3847/1538-4357/834/1/85)
- Notsu, Y., Honda, S., Maehara, H., et al. 2015, *PASJ*, 67, 33, doi: [10.1093/pasj/psv002](https://doi.org/10.1093/pasj/psv002)
- Noyes, R. W. 1996, in *Astronomical Society of the Pacific Conference Series*, Vol. 109, *Cool Stars, Stellar Systems, and the Sun*, ed. R. Pallavicini & A. K. Dupree, 3
- Noyes, R. W., Hartmann, L. W., Baliunas, S. L., Duncan, D. K., & Vaughan, A. H. 1984a, *ApJ*, 279, 763, doi: [10.1086/161945](https://doi.org/10.1086/161945)
- Noyes, R. W., Weiss, N. O., & Vaughan, A. H. 1984b, *ApJ*, 287, 769, doi: [10.1086/162735](https://doi.org/10.1086/162735)
- Oliphant, T. E. 2007, *Computing in Science & Engineering*, 9, 10, doi: [10.1109/MCSE.2007.58](https://doi.org/10.1109/MCSE.2007.58)
- Radick, R. R., Lockwood, G. W., Henry, G. W., Hall, J. C., & Pevtsov, A. A. 2018, *ApJ*, 855, 75, doi: [10.3847/1538-4357/aaae3](https://doi.org/10.3847/1538-4357/aaae3)
- Reinhold, T., Cameron, R. H., & Gizon, L. 2017, *A&A*, 603, A52, doi: [10.1051/0004-6361/201730599](https://doi.org/10.1051/0004-6361/201730599)
- Reinhold, T., Shapiro, A. I., Solanki, S. K., et al. 2020, *Science*, 368, 518, doi: [10.1126/science.aay3821](https://doi.org/10.1126/science.aay3821)
- Ricker, G. R., Winn, J. N., Vanderspek, R., et al. 2015, *Journal of Astronomical Telescopes, Instruments, and Systems*, 1, 014003, doi: [10.1117/1.JATIS.1.1.014003](https://doi.org/10.1117/1.JATIS.1.1.014003)
- Saar, S. H., & Donahue, R. A. 1997, *ApJ*, 485, 319, doi: [10.1086/304392](https://doi.org/10.1086/304392)
- Saar, S. H., & Schrijver, C. J. 1987, in *Lecture Notes in Physics*, Vol. 291, *Cool Stars, Stellar Systems and the Sun*, ed. J. L. Linsky & R. E. Stencel (Springer), 38–40, doi: [10.1007/3-540-18653-0_102](https://doi.org/10.1007/3-540-18653-0_102)
- Salabert, D., García, R. A., Beck, P. G., et al. 2016, *A&A*, 596, A31, doi: [10.1051/0004-6361/201628583](https://doi.org/10.1051/0004-6361/201628583)
- Schaefer, B. E., King, J. R., & Deliyannis, C. P. 2000, *ApJ*, 529, 1026, doi: [10.1086/308325](https://doi.org/10.1086/308325)
- Schrijver, C. J. 1987, *A&A*, 172, 111
- Shibayama, T., Maehara, H., Notsu, S., et al. 2013, *ApJS*, 209, 5, doi: [10.1088/0067-0049/209/1/5](https://doi.org/10.1088/0067-0049/209/1/5)
- Soderblom, D. R., Stauffer, J. R., Hudon, J. D., & Jones, B. F. 1993, *ApJS*, 85, 315, doi: [10.1086/191767](https://doi.org/10.1086/191767)
- Sowmya, K., Shapiro, A. I., Witzke, V., et al. 2021, *ApJ*, 914, 21, doi: [10.3847/1538-4357/abf247](https://doi.org/10.3847/1538-4357/abf247)
- Stoughton, C., Lupton, R. H., Bernardi, M., et al. 2002, *AJ*, 123, 485, doi: [10.1086/324741](https://doi.org/10.1086/324741)
- Tu, Z.-L., Yang, M., Wang, H. F., & Wang, F. Y. 2021, *ApJS*, 253, 35, doi: [10.3847/1538-4365/abda3c](https://doi.org/10.3847/1538-4365/abda3c)
- van der Walt, S., Colbert, S. C., & Varoquaux, G. 2011, *Computing in Science & Engineering*, 13, 22, doi: [10.1109/MCSE.2011.37](https://doi.org/10.1109/MCSE.2011.37)
- Vaughan, A. H., Preston, G. W., & Wilson, O. C. 1978, *PASP*, 90, 267, doi: [10.1086/130324](https://doi.org/10.1086/130324)
- Virtanen, P., Gommers, R., Oliphant, T. E., et al. 2020, *Nature Methods*, 17, 261, doi: [10.1038/s41592-019-0686-2](https://doi.org/10.1038/s41592-019-0686-2)
- Wang, S., Bai, Y., He, L., & Liu, J. 2020, *ApJ*, 902, 114, doi: [10.3847/1538-4357/abb66d](https://doi.org/10.3847/1538-4357/abb66d)
- Wang, S., Zhang, H.-T., Bai, Z.-R., et al. 2021, *Research in Astronomy and Astrophysics*, 21, 292, doi: [10.1088/1674-4527/21/11/292](https://doi.org/10.1088/1674-4527/21/11/292)
- Wilson, O. C. 1963, *ApJ*, 138, 832, doi: [10.1086/147689](https://doi.org/10.1086/147689)
- . 1968, *ApJ*, 153, 221, doi: [10.1086/149652](https://doi.org/10.1086/149652)
- . 1978, *ApJ*, 226, 379, doi: [10.1086/156618](https://doi.org/10.1086/156618)
- Wright, N. J., & Drake, J. J. 2016, *Nature*, 535, 526, doi: [10.1038/nature18638](https://doi.org/10.1038/nature18638)
- Wu, Y., Luo, A. L., Li, H.-N., et al. 2011, *Research in Astronomy and Astrophysics*, 11, 924, doi: [10.1088/1674-4527/11/8/006](https://doi.org/10.1088/1674-4527/11/8/006)
- Wu, Y., Chen, H., Tian, H., et al. 2022, *ApJ*, 928, 180, doi: [10.3847/1538-4357/ac5897](https://doi.org/10.3847/1538-4357/ac5897)
- Yan, Y., He, H., Li, C., et al. 2021, *MNRAS*, 505, L79, doi: [10.1093/mnras/505/1/79](https://doi.org/10.1093/mnras/505/1/79)
- Zhang, J., Zhao, J., Oswald, T. D., et al. 2019, *ApJ*, 887, 84, doi: [10.3847/1538-4357/ab4efe](https://doi.org/10.3847/1538-4357/ab4efe)
- Zhang, J., Bi, S., Li, Y., et al. 2020a, *ApJS*, 247, 9, doi: [10.3847/1538-4365/ab6165](https://doi.org/10.3847/1538-4365/ab6165)
- Zhang, J., Shapiro, A. I., Bi, S., et al. 2020b, *ApJL*, 894, L11, doi: [10.3847/2041-8213/ab8795](https://doi.org/10.3847/2041-8213/ab8795)
- Zhao, G., Zhao, Y.-H., Chu, Y.-Q., Jing, Y.-P., & Deng, L.-C. 2012, *Research in Astronomy and Astrophysics*, 12, 723, doi: [10.1088/1674-4527/12/7/002](https://doi.org/10.1088/1674-4527/12/7/002)
- Zhao, J. K., Oswald, T. D., Zhao, G., et al. 2013, *AJ*, 145, 140, doi: [10.1088/0004-6256/145/5/140](https://doi.org/10.1088/0004-6256/145/5/140)
- Zhao, J.-K., Oswald, T. D., Chen, Y.-Q., et al. 2015, *Research in Astronomy and Astrophysics*, 15, 1282, doi: [10.1088/1674-4527/15/8/013](https://doi.org/10.1088/1674-4527/15/8/013)
- Zong, W., Fu, J.-N., De Cat, P., et al. 2018, *ApJS*, 238, 30, doi: [10.3847/1538-4365/aadf81](https://doi.org/10.3847/1538-4365/aadf81)
- . 2020, *ApJS*, 251, 15, doi: [10.3847/1538-4365/abbb2d](https://doi.org/10.3847/1538-4365/abbb2d)